



Contents lists available at ScienceDirect



# Mechanism and Machine Theory

journal homepage: [www.elsevier.com/locate/mechmachtheory](http://www.elsevier.com/locate/mechmachtheory)



## Research paper

# Optimal design and comparative study of two antagonistically actuated tensegrity joints

Vimalesh Muralidharan<sup>a</sup>, Philippe Wenger<sup>b,\*</sup>

<sup>a</sup> École Centrale de Nantes, Laboratoire des Sciences du Numérique de Nantes (LS2N), Nantes 44321, France

<sup>b</sup> Centre National de la Recherche Scientifique (CNRS), LS2N, Nantes 44321, France

## ARTICLE INFO

### Article history:

Received 22 October 2020

Revised 23 December 2020

Accepted 8 January 2021

Available online 23 January 2021

### Keywords:

Revolute joint

Anti-parallelogram joint

Tensegrity

Antagonistic forces

Wrench-feasible workspace

Stiffness

Feasible design space

Optimal design

## ABSTRACT

This paper proposes design strategies and a comparative study of two antagonistically actuated tensegrity joints: a revolute (R) joint and an anti-parallelogram (X) joint. Geometrically, the R-joint has a fixed center of rotation while the X-joint has a moving center of rotation. Both joints are equipped with two lateral springs and are actuated by cables passing through these springs. Such tensegrity joints can be of interest for developing lightweight manipulators. They are designed to reach a prescribed wrench-feasible workspace (WFW) with a minimum desired stiffness throughout. The design strategy relies on the determination of the complete feasible design space for the problem, rather than resorting to a numerical optimizer for a particular solution. This approach provides more insight into the problem and also presents the designer with all the feasible designs. Several case studies are considered with different WFW specifications and design objectives for the R- and X-joints. The optimal designs obtained for the two joints are compared in terms of their actuation forces, stiffness, geometry, and mass.

© 2021 Elsevier Ltd. All rights reserved.

## 1. Introduction

There has been a growing interest in the robotics community to develop robot manipulators that are lightweight and energy-efficient. In this regard, the conventional serial architectures of robots are not ideal as they carry heavy moving masses, in the form of actuator units at each of the joints. As an alternative, the parallel manipulators are better, since the actuators are generally fixed at the base, while the links and passive joints constitute the moving masses. A class of parallel manipulators, namely the cable driven parallel manipulators (out of scope of this work), where the actuated limbs are replaced by remotely actuated cables, are known to possess very high payload to weight ratio.

More recently, cable driven serial kinematic chains, which are devoid of actuators at the joints, but rather actuated by remote cables, have been considered in [1]. They are interesting solutions for a lightweight design with a large workspace, that also allows for interaction with the environment [2]. Applications of such robots include artificial hands [3], exoskeletons [4], and other medical assistance devices. Another avenue to reduce the weight of serial manipulators comes from the consideration of biologically inspired tensegrity systems. In such systems, all the components are loaded axially. Since most of the materials are known to have a better axial strength than bending strength, it suffices to have simple cross-sections, thereby making them lighter. In this work, two remotely actuated tensegrity joints, namely, a revolute (R) joint

\* Corresponding author.

E-mail addresses: [vimalesh.muralidharan@ls2n.fr](mailto:vimalesh.muralidharan@ls2n.fr) (V. Muralidharan), [philippe.wenger@ls2n.fr](mailto:philippe.wenger@ls2n.fr) (P. Wenger).

## Nomenclature

R-joint	Revolute joint
X-joint	Anti-parallelogram joint
DoF	Degree(s)-of-freedom
WFW	Wrench-feasible workspace
3D	Three-dimensional
$\rho$	Linear mass density
$k$	Spring constant
$g$	Acceleration due to gravity (9.8 m/s <sup>2</sup> )
$M$	Point mass payload for a joint
$d$	Payload offset from the top bar of a joint
$F_1, F_2$	Actuation forces on a joint
$F_{\max}$	Upper bound on actuation forces
$K_r, K_x$	Stiffness of the R-joint, X-joint
$\underline{K}$	Minimum desired stiffness specification for a joint
$\theta_r, \theta_x$	Orientation of the R-joint, X-joint w.r.t. vertical
$\theta_{rm}, \theta_{xm}$	Positive boundary of the wrench-feasible workspace of R-joint, X-joint
$\theta_{\max}$	Generalization of $\theta_{rm}$ and $\theta_{xm}$
$r$	Semi-base length of R-joint
$h$	Height of the isosceles triangle in R-joint
$\eta$	Ratio ( $r/h$ )
$b$	Length of base and top bars of X-joint
$l$	Length of crossed bars of X-joint
$\lambda$	Ratio ( $l/b$ )
$c$	Short notation of $\cos \frac{\theta_{rm}}{2}$ and $\cos \frac{\theta_r}{2}$ (resp. $\cos \theta_{xm}$ and $\cos \theta_x$ ) for R-joint (resp. X-joint)
$s$	Short notation of $\sin \frac{\theta_{rm}}{2}$ and $\sin \frac{\theta_r}{2}$ (resp. $\sin \theta_{xm}$ and $\sin \theta_x$ ) for R-joint (resp. X-joint)
$C$	$2k(r^2 - h^2) - g\{M(d + h) + h\rho(\sqrt{h^2 + r^2} + 2r)\}$
$C_1$	$2(b^2 k - Mgd)$
$C_2$	$bg\{M + \rho(b + l)\}$
$\bar{t}$	Upper bound of $t$
$\underline{t}$	Lower bound of $t$

(see Fig. 1(a)), and an anti-parallelogram (X) joint (see Fig. 1(b)) are proposed as potential alternatives to the conventional joints in robot manipulators.

Remote actuation by cables requires such joints to be redundantly and antagonistically actuated with a number of motors greater than their respective degree(s)-of-freedom (DoF). The use of redundant actuators, despite making them expensive candidates, facilitates them with the property of variable stiffness. This makes it possible to develop robot manipulators suitable for both high stiffness (e.g., machining) and low stiffness (e.g., performing safe interactions) tasks. Several studies have been conducted recently on the variable stiffness joints/mechanisms. An antagonistically actuated cable-driven mechanism is proposed as a variable stiffness element for vibration control applications in [5]. It has been shown with a numerical example that in certain conditions the variable stiffness element can be more effective than passive stiffness components, for these applications. A synthesis method for designing variable stiffness components by using prestressed elastic elements has been proposed and illustrated with several joints by Boehler et al. in [6]. This method is focused on achieving the desired stiffness behavior at/near the unloaded configuration by modifying the springs' attachment points and their prestress properties. It is noted that no actuators have been considered for the movement of the joints in [6], thereby differentiating it from this work. In [7], a complete review of variable stiffness actuators is presented. Several methods for achieving variable stiffness and their respective applications have been detailed. This paper falls into the category of antagonistic motor setup, but with one significant difference. In [7], the springs are considered to be attached in series between the link and the actuating cable, whereas in this work the springs are arranged in parallel with the actuating cables (see Fig. 1). This arrangement is chosen because it ensures that the joints remain stiff/stable even in the absence of the actuation forces.

The use of R-joint is very common in robotics due to its simplicity in design and ease of manufacture. Apart from its conventional use in robotics, it has been used for modeling biological systems, such as the vertebrae of a fish in [8]. Some studies have considered an embedded actuation of the R-joint, where a prismatic actuator is used in series with a spring to control its orientation. Among them, the stiffness characteristics of the joint and its dependence on geometry were studied in [9]. Stiffness of the R-joint due to the actuators (named as active stiffness) and conditions for it to be negative were

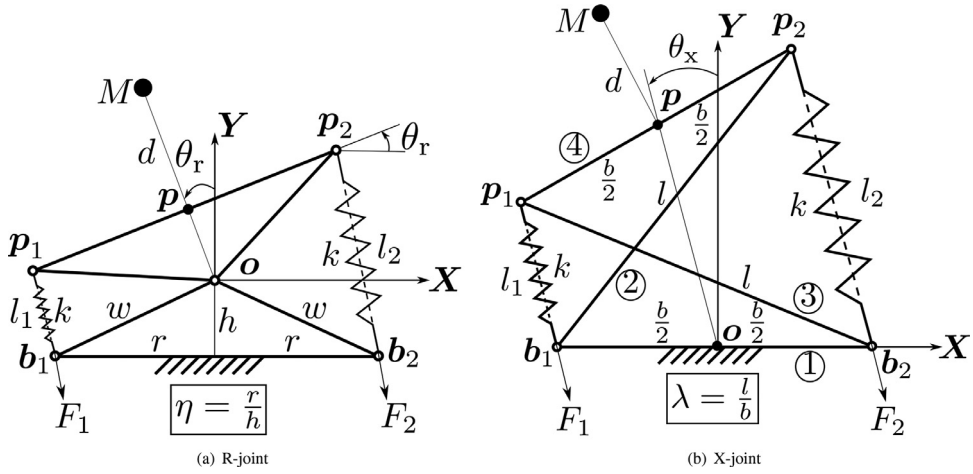


Fig. 1. Schematics of the joints under study: R-joint (left) and X-joint (right).

presented in [10]. A design methodology to maximize the proportion of active stiffness in the total stiffness of R-joint was proposed in [11].

On the other hand, the X-joint is not very popular as a joint in the robotics community. The X-shaped tensegrity structure was originally conceived by Snellson [12] and gained popularity among artists and architects for building stable structures [13]. More recently, several 1-DoF and 2-DoF tensegrity mechanisms have been developed based on the X-shaped model in [14,15]. The X-joint has also found applications in the model of a knee in [16], gear trains in [17], and bird neck in [18]. A complete study of workspace, kinematics, and statics of a 2-X manipulator composed of two X-joints stacked one above the other, has been conducted in [19]. It was illustrated with an example that the redundancy in actuation, due to the use of four cables, can be exploited to obtain a variable stiffness within its wrench-feasible workspace (WFW). This makes the manipulator suitable for high stiffness tasks (such as drilling), while performing safe interactions with the environment when needed. A tentative design optimization scheme of X-joints to be used in a bird neck model was proposed in [20]. The optimization was conducted in a numerical, iterative way in order to maximize the WFW and to ensure a stable configuration at rest, while the maximal actuation force was fixed. In contrast, this paper deals with the converse problem, where the joints are designed to possess a fixed WFW with a minimum desired stiffness throughout, and the maximal actuation force is considered as a candidate design objective. Additionally, an algebraic approach is proposed for the resolution of the problem at hand, while a numerical strategy was followed in [20]. Very recently, the 2-X manipulator with offsets between the joints was studied in [21]. It was shown that the manipulator with X-joints possesses a significantly larger workspace than the conventional 2-R manipulator, when identical limits are imposed on the joint motions.

A comparative study of the R- and X- joints, designed to possess an identical WFW with the same stiffness values at rest and at WFW boundary, has been presented by the authors in [22]. Such a design process would be useful in developing bio-mimicking mechanisms where the desired stiffness values might be known exactly at the center and bounds of the WFW. However, in this paper, we are interested in a more general problem, in which the two joints are designed to possess a stiffness greater than or equal to a user-specified value throughout the WFW. Such a requirement is often encountered in developing robot manipulators for machining tasks such as drilling, where the exact stiffness values might not be known, but an estimate of the minimum desired stiffness might be known. It is found that this problem is more complicated and delves into several cases and sub-cases for its resolution. Nevertheless, the proposed design strategies are carried out by deriving algebraic expressions of the constraints and of the objective functions. This approach allows us to characterize the complete feasible design space and to determine optimal solutions directly without resorting to numerical optimization techniques.

The major contributions of this work may be summarized as follows:

- Strategies to obtain the complete feasible design space for the R- and X- joints, while they are designed to possess a user-specified WFW with a minimum desired stiffness throughout, are presented.
- Selection of the optimal design is illustrated for different design objectives, specifically, minimization of maximal actuation force and total joint mass.
- A comparative study on the performance of the optimal designs of R- and X- joints is carried out in terms of stiffness, geometry, actuation forces, and masses with several numerical examples. General guidelines are presented on the choice of these joints for different WFW and stiffness requirements.

The rest of this paper is organized as follows: the static models of the R- and X- joints are presented in Section 2, the conditions for design of these joints are listed in Section 3. It is remarked that parts of Sections 2 and 3, on the derivation

of static models can also be found in the authors' previous publication [22]. A strategy to obtain the feasible design space and the optimal design is developed for R-joint in Section 4 and for X-joint in Section 5. A comparative study on the performance of these joints is conducted with several numerical examples in Section 6. The effects of mass density, payload parameters, and spring free-length are discussed in Sections 7 and 8. Finally, the conclusions of this study are reported in Section 9.

## 2. Static analysis of the joints

The schematic diagrams of the R-joint and the X-joint under study are shown in Figs. 1(a) and (b), respectively.

The R-joint is composed of two congruent isosceles triangles (made of three bars), one on top of the other, connected by a revolute joint at  $\mathbf{o}$ . The geometry of these triangles is defined by the semi-base length ( $r$ ) and height ( $h$ ). The orientation of this joint is measured by the angle ( $\theta_r$ ) between the upper triangle and the vertical as shown in Fig. 1(a).

The X-joint is composed of three moving links 2, 3, 4 and a fixed link 1, each connected to its neighbors with a revolute joint. The links 1 and 4 are each of length  $b$ , while the other two links are of length  $l$ . The orientation of this joint is measured by the angle ( $\theta_x$ ) between the segment joining the midpoints of links 1 and 4, and the vertical as shown in Fig. 1(b). It is noted that the condition ( $l > b$ ) is necessary for the assembly of the X-joint. Collisions between the links can be avoided by arranging them in different layers (see [18]).

Each joint is equipped with a pair of identical springs with spring constant  $k$ , to impart stiffness into the system. The free-lengths of the springs are assumed to be zero in this study. While the physical length of the spring cannot be zero, it is possible to achieve an effective zero free-length with guiding systems and pulleys between the spring and the attachment points (see, e.g., [23,24]). Nevertheless, the effect of non-zero free-length has been discussed briefly in Section 8.

To take into account a payload or the mass of subsequent joint(s) stacked overhead, a point mass  $M$  is considered to be linked to the segment  $\mathbf{p}_1\mathbf{p}_2$  (without any rigid connections) at a distance  $d$ . The linear mass density (i.e., mass per unit length) of all links and bars (indicated by thick lines in Fig. 1) is given by  $\rho$ . Finally, the joints are actuated antagonistically by cables passing through the springs, imparting forces  $F_1$  and  $F_2$ , respectively, as shown in Fig. 1. The presence of two actuating cables makes the joints redundantly actuated, but allows for a range of possible stiffnesses at any given orientation as explained in the following sections.

It is remarked that the proposed joints qualify as tensegrity joints because it can be shown that all the bars, springs, and cables experience only *external* axial loading in static equilibrium. However, there is one minor difference with the conventional use of the term "tensegrity", where all the rigid elements (bars) must be loaded in compression, rather than in tension. It can be shown that the top bars linking  $\mathbf{p}_1\mathbf{p}_2$  in the two joints are in tension, suggesting that their replacement with a cable is potentially possible. But, rigid bars have been chosen against the tensegrity paradigm and despite the additional mass incurred, for two reasons. Firstly, to ensure that the joints have just one DoF like the conventional robotic joints and secondly, to cope with the compression loads that are known to arise when the dynamic effects (out of scope of this paper) are considered.

### 2.1. Static equilibrium and stiffness of the R-joint

From Fig. 1(a), the coordinates  $l_1$  and  $l_2$  can be expressed in terms of  $\theta_r$  as follows:

$$l_1 = 2 \left( h \cos \frac{\theta_r}{2} - r \sin \frac{\theta_r}{2} \right), \quad l_2 = 2 \left( h \cos \frac{\theta_r}{2} + r \sin \frac{\theta_r}{2} \right) \quad (1)$$

The rotation range of the R-joint is limited by singularities due to the actuating cables, in two different ways. Firstly, due to the occurrence of *force-closure singularity* (see [25]), when the points  $\mathbf{b}_i$ ,  $\mathbf{o}$ , and  $\mathbf{p}_i$  ( $i = 1$  or  $2$ ) become collinear. Secondly, due to the vanishing of  $l_1$  or  $l_2$ , where the direction of force applied by the respective cable becomes ill-defined. It can be shown that the limit of motion is due to force-closure singularity when  $r < h$  and due to vanishing of  $l_i$  ( $i = 1, 2$ ) when  $r > h$ . The rotation range depends on the link lengths and reaches its maximum amplitude  $[-\frac{\pi}{2}, \frac{\pi}{2}]$  when  $r = h$  (see [26] for more details).

The total potential energy of the R-joint, due to gravity (considering the zero potential along X-axis), springs, and external forces applied by the cables, is obtained to be:

$$U_r = \rho g h \left( 2r + \sqrt{r^2 + h^2} \right) \cos \theta_r + Mg(d + h) \cos \theta_r + 2k \left\{ r^2 + h^2 - (r^2 - h^2) \cos \theta_r \right\} + F_1 l_1 + F_2 l_2 \quad (2)$$

where  $g$  is the acceleration due to gravity. Differentiation of the total potential energy of the joint w.r.t.  $\theta_r$  yields the equation of static equilibrium, which is of the form:  $G_r = \Gamma_r$ , where,

$$G_r = C \sin \theta_r, \quad \text{with } C = 2k(r^2 - h^2) - g \left\{ M(d + h) + h\rho \left( \sqrt{h^2 + r^2} + 2r \right) \right\} \quad (3)$$

$$\Gamma_r = -F_1 \frac{dl_1}{d\theta_r} - F_2 \frac{dl_2}{d\theta_r} \quad (4)$$

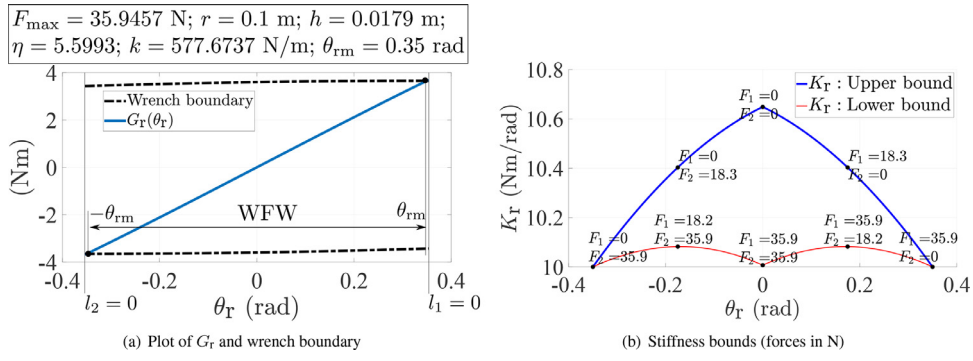


Fig. 2. WFW (left) and stiffness bounds (right) for the R-joint.

The symbol  $G_{\Gamma}$  represents the wrench due to gravity and springs, while  $\Gamma_{\Gamma}$  represents the external wrench applied by the cables. The forces provided by the cables are limited physically, leading to:  $F_1, F_2 \in [F_{\min}, F_{\max}]$ . From the expressions of  $l_1$  and  $l_2$  in Eq. (1), it can be shown that the coefficient of  $F_1$  (resp.  $F_2$ ) in  $\Gamma_{\Gamma}$  (see Eq. (4)) is positive (resp. negative) inside the range of motion limited by singularities. Thus, the external wrench  $\Gamma_{\Gamma}$  is bounded above (resp. below) by  $\Gamma_{\max}$  (resp.  $\Gamma_{\min}$ ), which occurs when  $F_1 = F_{\max}$  and  $F_2 = F_{\min}$  (resp.  $F_1 = F_{\min}$  and  $F_2 = F_{\max}$ ). As a consequence of these bounds on  $\Gamma_{\Gamma}$ , the equilibrium equation can be satisfied only when:  $G_{\Gamma} \in [\Gamma_{\min}, \Gamma_{\max}]$ . The range of  $\theta_{\Gamma} \in [-\theta_{rm}, \theta_{rm}]$  within which this condition is valid is the WFW for the R-joint. As a numerical illustration, consider the following data from Section 4.4:  $\rho = 0.2121 \text{ Kg/m}$ ,  $M = 0.2 \text{ Kg}$ ,  $d = 0.25 \text{ m}$ ,  $r = 0.1 \text{ m}$ ,  $h = 0.0179 \text{ m}$ ,  $k = 577.6737 \text{ N/m}$ , and  $F_{\max} = 35.9457 \text{ N}$ . The corresponding plot of wrench boundaries ( $\Gamma_{\min}, \Gamma_{\max}$ ) and curve  $G_{\Gamma}$  are shown in Fig. 2(a). It is observed that the WFW is bounded by the intersection of  $G_{\Gamma}$  with the wrench boundaries.

The joint stiffness ( $K_{\Gamma}$ ) is derived upon computing the second derivative of the total potential energy w.r.t.  $\theta_{\Gamma}$ . The resulting expression is:

$$K_{\Gamma} = C \cos \theta_{\Gamma} + \frac{1}{2} F_1 \left( -h \cos \frac{\theta_{\Gamma}}{2} + r \sin \frac{\theta_{\Gamma}}{2} \right) - \frac{1}{2} F_2 \left( h \cos \frac{\theta_{\Gamma}}{2} + r \sin \frac{\theta_{\Gamma}}{2} \right) \quad (5)$$

It is essential to account for the static equilibrium equation ( $G_{\Gamma} = \Gamma_{\Gamma}$ ) while evaluating the stiffness of the joint. Since the R-joint is redundantly actuated with two cables, there exists an  $\infty^1$  combination of forces satisfying the equilibrium equation at a given orientation. These combinations enable the joint to exhibit a range of stiffness values at that orientation. The expression for lower boundary of stiffness as a function of  $\theta_{\Gamma}$  has been derived in Appendix A.2 (see Eq. (A.8)). A similar result for the upper boundary of stiffness can also be obtained, following the same procedure. As a numerical example, the stiffness bounds for the joint parameters listed in Fig. 2(a), are shown in Fig. 2(b). The corresponding force values are also indicated on the boundaries.

## 2.2. Static equilibrium and stiffness of the X-joint

From Fig. 1(b),  $l_1$  and  $l_2$  can be obtained in terms of  $\theta_X$  as:

$$l_1 = -b \sin \theta_X + \sqrt{l^2 - b^2 \cos^2 \theta_X}, \quad l_2 = b \sin \theta_X + \sqrt{l^2 - b^2 \cos^2 \theta_X} \quad (6)$$

The singularities that limit the motion of the X-joint occur at  $\theta_X = \pm \frac{\pi}{2}$ , irrespective of the dimensions of the links. At these configurations the entire joint folds flat on a single line.

The total potential energy of the X-joint is computed in a manner similar to that of the R-joint as:

$$U_X = -\cos 2\theta_X (b^2 k - dgM) + \{\rho(b+l) + M\}g \cos \theta_X \sqrt{l^2 - b^2 \cos^2 \theta_X} + kl^2 + F_1 l_1 + F_2 l_2 \quad (7)$$

The static equilibrium equation is obtained upon differentiation of the total potential energy of the joint w.r.t.  $\theta_X$  as:  $G_X = \Gamma_X$ , where:

$$\left\{ \begin{array}{l} G_X = C_1 \sin 2\theta_X + \frac{C_2 \sin \theta_X (2b^2 \cos^2 \theta_X - l^2)}{b \sqrt{l^2 - b^2 \cos^2 \theta_X}}, \\ \text{with } C_1 = 2(b^2 k - Mgd), C_2 = bg\{M + \rho(b+l)\} \end{array} \right. \quad (8)$$

$$\Gamma_X = -F_1 \frac{dl_1}{d\theta_X} - F_2 \frac{dl_2}{d\theta_X} \quad (9)$$

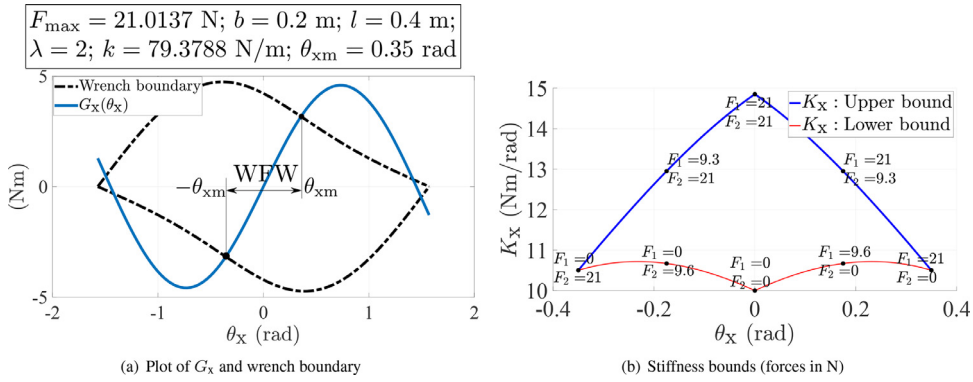


**Fig. 3.** WFW (left) and stiffness bounds (right) for the X-joint.

The symbols  $G_X$  and  $\Gamma_X$  possess the same physical meaning as  $G_\Gamma$  and  $\Gamma_\Gamma$ , respectively and the bounds of  $\Gamma_X$  are reached for the same force bounds as for the R-joint. The joint stiffness is obtained from the second derivative of the total potential function w.r.t.  $\theta_X$ . The corresponding expression is:

$$K_X = 2C_1 \cos 2\theta_X - \frac{C_2 \cos \theta_X \left\{ (l^2 - b^2 \cos 2\theta_X)^2 - b^2(l^2 - b^2) \cos 2\theta_X \right\}}{b(l^2 - b^2 \cos^2 \theta_X)^{3/2}} + bF_1 \left( \frac{bl^2 \cos 2\theta_X - b^3 \cos^4 \theta_X}{(l^2 - b^2 \cos^2 \theta_X)^{3/2}} + \sin \theta_X \right) + bF_2 \left( \frac{bl^2 \cos 2\theta_X - b^3 \cos^4 \theta_X}{(l^2 - b^2 \cos^2 \theta_X)^{3/2}} - \sin \theta_X \right) \quad (10)$$

As a numerical illustration, the data from Section 5.4 have been considered:  $\rho = 0.2121$  Kg/m,  $M = 0.2$  Kg,  $d = 0.25$  m,  $b = 0.2$  m,  $l = 0.4$  m,  $k = 79.3788$  N/m, and  $F_{max} = 21.0137$  N. As in the case of R-joint, the WFW and the stiffness bounds for the X-joint are presented in Fig. 3. From Fig. 3(a), it is observed that the WFW is formed by three disconnected regions,  $\theta_{xm} \in [-\theta_{xm}, \theta_{xm}]$  and two smaller isolated regions near the flat singularities ( $\theta_X = \pm \frac{\pi}{2}$ ). A “jump” from one region to another could be possible with a suitable dynamic trajectory as shown in [27], but those isolated regions are very small and are associated with unstable equilibrium configurations or negative stiffness. Thus, only the central portion would be considered as the WFW of this joint, in further study. The stiffness bounds of this joint are plotted for  $\theta_X \in [-\theta_{xm}, \theta_{xm}]$  in Fig. 3(b).

### 3. Feasible designs of the joints for a specified WFW and a minimum stiffness

In this study, the link lengths and the spring constant of the joints are considered to be the design variables, while the linear mass density and payload characteristics ( $\rho, M, d$ ) are treated as parameters whose values are known *a priori*. The maximal force required to move the joint, referred to as  $F_{max}$ , is treated as a design variable, though it can also be considered as an objective function. In this study, the joints will be designed to possess a user-specified WFW with a minimum desired stiffness throughout. Such a design process will be useful for developing robot manipulators with a desired workspace size and stiffness requirements for machining applications (e.g., drilling). Other potential applications include development of bio-mimicking systems and exoskeletons where the desired range of motion and stiffness characteristics (in some cases) for each of its joints are known beforehand.

The goal is to find optimal designs of the joints, such that the following conditions are met:

- The joint should possess the specified WFW of the general form:  $[-\theta_{max}, \theta_{max}]$  with  $\theta_{max} < \frac{\pi}{2}$  to avoid singularities.
- The joint stiffness must be greater than or equal to a specified value of  $K(> 0)$  throughout the WFW for all admissible values of forces satisfying the equation of static equilibrium.
- The bounds on link lengths and spring constant must be respected.

Due to symmetry of the joints about their respective zero orientations, ensuring  $[0, \theta_{max}] \in$  WFW, ensures that  $[-\theta_{max}, 0] \in$  WFW. Similar arguments can be made about the stiffness behavior of the joints as well. This makes it sufficient to study just one half of the problem, i.e.,  $\theta_\Gamma > 0$  and  $\theta_X > 0$ . In the following, the positive boundary of WFW is denoted by  $\theta_{rm}$  for the R-joint and  $\theta_{xm}$  for the X-joint.

In accordance with the conditions listed above, several equations and inequalities have been formulated for the two joints as shown in Table 1 (assuming  $F_{min} = 0$ ). Physically, the first two conditions ensure that no singularities occur within the WFW and that the positive boundary of the WFW is formed by the intersection of the curves  $G_\Gamma$  (resp.  $G_X$ ) and  $\Gamma_{max}$  (see [26] for more details).

**Table 1**

Formulation of the stipulated conditions for the design of R-joint and X-joint.

R-joint	X-joint
$\begin{cases} l_1(\theta_{rm}) > 0, \text{ if } (r > h) \\ l_2(\theta_{rm}) < 2w, \text{ if } (r < h) \end{cases}$	No singularities when $\left(\theta_{xm} < \frac{\pi}{2}\right)$ (12a)
$G_r(\theta_{rm}) + F_{\max} \frac{dl_1}{d\theta_r}(\theta_{rm}) = 0$	$G_x(\theta_{xm}) + F_{\max} \frac{dl_1}{d\theta_x}(\theta_{xm}) = 0$ (12b)
$K_r(\theta_r = 0, F_1 = F_{\max}, F_2 = F_{\max}) \geq K$	$K_x(\theta_x = 0, F_1 = 0, F_2 = 0) \geq K$ (12c)
$K_r(\theta_r = \theta_{rm}, F_1 = F_{\max}, F_2 = 0) \geq K$	$K_x(\theta_x = \theta_{rm}, F_1 = F_{\max}, F_2 = 0) \geq K$ (12d)
$0 \leq k \leq \bar{k}$	$0 \leq k \leq \bar{k}$ (12e)
$\underline{r} \leq r \leq \bar{r}$	$\underline{b} \leq b \leq \bar{b}$ (12f)
$\underline{w} \leq w \leq \bar{w}$	$\underline{l} \leq l \leq \bar{l}$ (12g)

Before proceeding further, two important results are stated:

- The actuation forces have a negative (resp. positive) impact on the stiffness of the R-joint (resp. X-joint).
- The least value of stiffness, when it is imposed to be positive, occurs at the zero orientation or at the boundary of the WFW for both joints.

Proofs of these results can be found in [Appendix A](#) for the R-joint and [Appendix B](#) for the X-joint. Using them, the third and fourth conditions in [Table 1](#) have been included to ensure that the lower boundary of stiffness remains greater than or equal to the stipulated value of  $K$ .

The last three conditions on geometry and spring constant of the joints have been imposed due to practical considerations, such as, availability of corresponding components in the market and ease of fabrication/assembly.

Finally, the ratio of link lengths:  $\eta (= \frac{r}{h})$  for the R-joint and  $\lambda (= \frac{l}{b})$  for the X-joint have been introduced into the formulation, eliminating the variables  $h$  and  $l$ , respectively. This is because the ratio provides more insight into the problem and also simplifies the resulting expressions considerably.

The design problem involves four design variables, namely,  $(\eta, r, F_{\max}, k)$  for R-joint and  $(\lambda, b, F_{\max}, k)$  for X-joint. It relies on one equation and six inequalities (see [Table 1](#)).

As a general strategy, the equation ([Eq. \(11b\)](#) for R-joint and [Eq. \(12b\)](#) for X-joint) will be used to eliminate  $k$ . Consequently, only the two geometric variables and the maximal actuation force  $F_{\max}$  remain, thereby making the design space three-dimensional (3D). Then, all the inequalities will be reduced to lower/upper bounds on  $F_{\max}$  or conditions involving only the geometric variables. This will allow us to build the *feasible geometric space* followed by the *feasible design space*, defined below.

- **Feasible geometric space:** The set of all  $(\eta, r)$  (resp.  $(\lambda, b)$ ) values for which at least one feasible design exists forms the feasible geometric space of the R-joint (resp. X-joint). It is computed as the intersection of all the inequalities that involve the geometric variables, but devoid of the maximal actuation force ( $F_{\max}$ ).
- **Feasible design space:** The set of all geometric and maximal force values which satisfy all the conditions in [Table 1](#), defines the complete feasible design space and is referred to as the feasible design space for the joints. Graphically, it can be obtained as the volume enclosed between the lower and upper boundaries of  $F_{\max}$  inside the feasible geometric space.

The steps involved in the construction of these design spaces are detailed for the two joints in the following.

#### 4. Complete feasible design space and design strategy for R-joint

A methodology is proposed to build the complete feasible design space of the R-joint satisfying the conditions listed in the left column of [Table 1](#). Firstly, these conditions are reduced to inequalities involving only  $(\eta, r, F_{\max})$  in [Section 4.1](#). This is followed by the computation of feasible geometric space  $(\eta, r)$  in [Section 4.2](#) and the feasible design space  $(\eta, r, F_{\max})$  in [Section 4.3](#). Finally, a strategy for the design of R-joint is presented with a numerical example in [Section 4.4](#).

##### 4.1. Treatment of the constraints involved in the design of R-joint

In this section, the substitutions:  $c = \cos \frac{\theta_{rm}}{2}$ ,  $s = \sin \frac{\theta_{rm}}{2}$ , have been incorporated to keep the resulting expressions compact. Since  $\theta_{rm} < \frac{\pi}{2}$ , it follows that  $c > s$ .

The conditions in [Eqs. \(11a\)-\(11g\)](#) are treated successively, in the following.

From Fig. 1(a), it follows that  $w = \sqrt{r^2 + h^2} = \frac{r\sqrt{\eta^2 + 1}}{\eta}$ . Substituting this expression for  $w$  and using the expressions of  $l_1, l_2$  from Eq. (1), the inequalities in Eq. (11a) lead to the following conditions:

$$\left\{ \begin{array}{l} l_1(\theta_{rm}) > 0 \Rightarrow \eta < \bar{\eta}, \text{ where } \bar{\eta} = \cot \frac{\theta_{rm}}{2}, \text{ if } (\eta > 1) \\ l_2(\theta_{rm}) < 2w \Rightarrow c - \sqrt{\eta^2 + 1} + \eta s < 0, \text{ if } (\eta < 1) \end{array} \right. \quad (13a)$$

$$\left\{ \begin{array}{l} l_1(\theta_{rm}) > 0 \Rightarrow \eta < \bar{\eta}, \text{ where } \bar{\eta} = \cot \frac{\theta_{rm}}{2}, \text{ if } (\eta > 1) \\ l_2(\theta_{rm}) < 2w \Rightarrow c - \sqrt{\eta^2 + 1} + \eta s < 0, \text{ if } (\eta < 1) \end{array} \right. \quad (13b)$$

Using the expressions in Eqs. (1) and (3), the condition in Eq. (11b) leads to:

$$F_{\max}r\left(c + \frac{s}{\eta}\right) - 2cCs = 0 \Rightarrow C = \frac{F_{\max}r(c\eta + s)}{2c\eta s} \quad (14)$$

Equating the above expression of  $C$  with the one in Eq. (3), and solving for  $k$  yields:

$$k = \frac{2cgs\left\{\eta M(d\eta + r) + \left(\sqrt{\eta^2 + 1} + 2\eta\right)\rho r^2\right\} + F_{\max}\eta r(c\eta + s)}{4c(\eta^2 - 1)r^2 s} \quad (15)$$

From the above expression of  $k$ , it is clear that  $(\eta > 1)$  is both necessary and sufficient for ensuring  $k > 0$ . Hence, from the results of the previous inequality, the one in Eq. (13a) must be considered. Thus, the condition  $(1 < \eta < \bar{\eta})$  must be carried throughout the problem.

Using Eq. (14) (resp. Eq. (15)),  $C$  (resp.  $k$ ) can be eliminated from the inequalities in Eqs. (11c) through (11g). Hence, in the design optimization problem of R-joint, the design space may be reduced to the span of two geometric variables  $(\eta, r)$  and the maximal actuation force  $F_{\max}$ .

The inequalities on stiffness (Eqs. (11c) and (11d)) and the bounds on  $(k, w)$  (Eqs. (11e) and (11g)) are reduced to conditions involving  $(\eta, r, F_{\max})$  in the following.

- Condition on joint stiffness in Eq. (11c):

Using the expression of stiffness from Eq. (5), the inequality in Eq. (11c) can be expanded as:

$$C - \frac{F_{\max}r}{\eta} - \underline{K} \geq 0 \quad (16)$$

Substituting for  $C$  from Eq. (14) and clearing the common denominator ( $> 0$ ), results in:

$$F_{\max}r(c\eta - 2cs + s) - 2c\eta \underline{K}s \geq 0 \quad (17)$$

The factor  $(c\eta - 2cs + s)$  in the coefficient of  $F_{\max}$ , can be rewritten as  $(c(\eta - s) + s(1 - c))$ . Recalling that  $\eta > 1$  and  $c, s \in [0, 1]$ , it follows that this factor is always positive. Hence, the inequality in Eq. (17) can be rewritten as a lower bound on  $F_{\max}$  as follows:

$$F_{\max} \geq \underline{F}_{K_1}, \text{ with } \underline{F}_{K_1} = \frac{2c\eta \underline{K}s}{r(c\eta - 2cs + s)} \quad (18)$$

- Condition on joint stiffness in Eq. (11d):

Using Eq. (5), the inequality in Eq. (11d) can be expanded into:

$$C(c^2 - s^2) + \frac{1}{2}F_{\max}r\left(s - \frac{c}{\eta}\right) - \underline{K} \geq 0 \quad (19)$$

Substituting for  $C$  from Eq. (14) and clearing the common denominator ( $> 0$ ) leads to:

$$F_{\max}r(c^3\eta - s^3) - 2c\eta \underline{K}s \geq 0 \quad (20)$$

Recalling that  $c > s$  and  $\eta > 1$ , the above inequality also leads to a lower bound on  $F_{\max}$ :

$$F_{\max} \geq \underline{F}_{K_2}, \text{ with } \underline{F}_{K_2} = \frac{2c\eta \underline{K}s}{r(c^3\eta - s^3)} \quad (21)$$

- Bounds on  $k$  in Eq. (11e):

Using Eq. (15), it has been shown that the condition for  $k$  to be positive is  $\eta > 1$ . Thus, only the upper bound on  $k$  remains to be considered, i.e.,  $k - \bar{k} \leq 0$ . Substituting for  $k$  from Eq. (15) and performing the standard simplifications, as above, results in:

$$2cgs\left\{\eta M(d\eta + r) + \left(\sqrt{\eta^2 + 1} + 2\eta\right)\rho r^2\right\} + F_{\max}\eta r(c\eta + s) - 4c(\eta^2 - 1)\bar{k}r^2 s \leq 0 \quad (22)$$

It is observed that the coefficient of  $F_{\max}$  is positive in this inequality. Hence, the above condition can be simplified to provide an upper bound for  $F_{\max}$  as follows:

$$F_{\max} \leq \bar{F}_k, \text{ where } \bar{F}_k = \frac{2cs\left[2(\eta^2 - 1)\bar{k}r^2 - g\left\{\eta M(d\eta + r) + \left(\sqrt{\eta^2 + 1} + 2\eta\right)\rho r^2\right\}\right]}{\eta r(c\eta + s)} \quad (23)$$

- Bounds on  $w$  in Eq. (11g):

Substituting  $w = \frac{r\sqrt{\eta^2+1}}{\eta}$  (see Fig. 1(a)) into the condition in Eq. (11g):

$$\underline{w} \leq \frac{r\sqrt{\eta^2+1}}{\eta} \leq \bar{w} \quad (24)$$

$$\Rightarrow \begin{cases} r \geq \underline{r}_w \\ r \leq \bar{r}_w \end{cases} \quad \text{with } \underline{r}_w = \frac{\underline{w}\eta}{\sqrt{\eta^2+1}} \text{ and } \bar{r}_w = \frac{\bar{w}\eta}{\sqrt{\eta^2+1}} \quad (25)$$

It is noted that the above conditions involve only  $(r, \eta)$ , and are devoid of  $F_{\max}$ .

The conditions derived above will be used to construct the feasible geometric space  $(\eta, r)$  for the R-joint, followed by the derivation of the bounds on  $F_{\max}$ , as detailed in the subsequent sections.

#### 4.2. Feasible geometric space $(\eta, r)$ of R-joint

Recalling that  $k$  is eliminated from the set of design variables using Eq. (15), the design space of the R-joint is only composed of  $\eta$ ,  $r$ , and  $F_{\max}$ . The intersection of all the conditions involving  $\eta$  and  $r$  must be first computed to form the feasible geometric space  $(\eta, r)$ . Thus, the bounds on  $r, w$ , and the condition  $(1 < \eta < \bar{\eta})$  are considered from Eqs. (11f), (25), and (15), respectively. In addition to these, two more conditions which stipulate that the upper bound of  $F_{\max}$ , i.e.,  $\bar{F}_k$ , remains greater than the lower bounds ( $\underline{F}_{K_1}$  and  $\underline{F}_{K_2}$ ), must also be considered. These two conditions are treated in the following.

##### 4.2.1. Treatment of $(\bar{F}_k \geq \underline{F}_{K_1})$

Starting with:

$$\bar{F}_k - \underline{F}_{K_1} \geq 0 \quad (26)$$

Substituting for  $\underline{F}_{K_1}$  and  $\bar{F}_k$  from Eqs. (18) and (23), results in:

$$\frac{2cs \left[ (-c\eta + 2cs - s) \left\{ g \left\{ \eta M(d\eta + r) + (\sqrt{\eta^2+1} + 2\eta)\rho r^2 \right\} - 2(\eta^2 - 1)\bar{k}r^2 \right\} - \eta^2 \underline{K}(c\eta + s) \right]}{\eta r(c\eta + s)(c\eta - 2cs + s)} \geq 0 \quad (27)$$

The last factor in the denominator,  $(c\eta - 2cs + s)$ , has been shown to be positive below Eq. (17). Also, recalling that  $c > 0$  and  $s > 0$ , it is clear that the remaining factors in the denominator and the first three factors in the numerator are also positive. This shows that the above inequality requires the last factor in the numerator to be positive, which can be rewritten as a quadratic inequality in  $r$  as follows:

$$A_{r_1}r^2 + B_{r_1}r + C_{r_1} \geq 0, \quad \text{where,} \quad (28)$$

$$\begin{cases} A_{r_1} = (c\eta - 2cs + s) \left\{ 2(\eta^2 - 1)\bar{k} - g(\sqrt{\eta^2+1} + 2\eta)\rho \right\} \\ B_{r_1} = -g\eta M(c\eta - 2cs + s) \\ C_{r_1} = -\eta^2 \{ dgM(c\eta - 2cs + s) + \underline{K}(c\eta + s) \} \end{cases} \quad (29)$$

From the above expressions, it is observed that:  $B_{r_1} < 0, C_{r_1} < 0$ . Thus, the condition  $(A_{r_1} > 0)$  is necessary for the inequality in Eq. (28) to be satisfied. This requires the last factor in  $A_{r_1}$  to be positive, which is treated further in Appendix C. The two resulting necessary conditions involving  $\eta, \bar{k}, \rho$ , and  $\theta_{rm}$  are listed below (see Appendix C for derivation):

$$P > \frac{(2c+1)s}{c^2 - s^2} \quad \text{where } P = \frac{2\bar{k}}{\rho g}, c = \cos \frac{\theta_{rm}}{2}, s = \sin \frac{\theta_{rm}}{2} \quad (30)$$

$$\begin{cases} (\eta^2 - 1)^2 P^2 + 3\eta^2 - 4(\eta^2 - 1)\eta P - 1 > 0 \\ \Rightarrow \eta > \underline{\eta}, \quad \text{where } \underline{\eta} \text{ is the largest root of the quartic polynomial} \end{cases} \quad (31)$$

When the above conditions are satisfied, it is ensured that  $(A_{r_1} > 0)$ . Thus, from the discussion in Appendix D, the inequality in Eq. (28) reduces to a lower bound on  $r$  as:

$$r \geq \underline{r}_{K_1}, \quad \text{where } \underline{r}_{K_1} = \frac{-B_{r_1} + \sqrt{B_{r_1}^2 - 4A_{r_1}C_{r_1}}}{2A_{r_1}} \quad (32)$$

with the expressions of  $A_{r_1}, B_{r_1}, C_{r_1}$  presented in Eq. (29).

#### 4.2.2. Treatment of $(\bar{F}_k \geq \underline{F}_{K_2})$

Similar to the previous case, the following result is obtained from  $(\bar{F}_k - \underline{F}_{K_2} \geq 0)$ :

$$r \geq r_{K_2}, \text{ where } r_{K_2} = \frac{-B_{r_2} + \sqrt{B_{r_2}^2 - 4A_{r_2}C_{r_2}}}{2A_{r_2}} \quad (33)$$

The expressions of  $A_{r_2}$ ,  $B_{r_2}$ ,  $C_{r_2}$  can be found in [Appendix E](#).

### 4.3. Bounds of $F_{\max}$ and the feasible design space for R-joint

In the previous section, the consideration of the constraints was shown to define bounds on the maximal forces that depend on the two geometric variables only. Altogether, those bounds along with the bounds on the geometric variables, define a 3D region in which every point corresponds to a feasible design associated with a maximal actuation force (see [Fig. 5\(c\)](#) further). Note that if the designer wants to minimize the maximal actuation force, the lower bound on  $F_{\max}$  defines the objective function and optimal design can be found directly on this surface.

Within the feasible geometric space, it is essential to identify which lower bound of  $F_{\max}$  ( $\underline{F}_{K_1}$  or  $\underline{F}_{K_2}$ ) must be considered for defining the lower boundary of the 3D volume. This requires a classification of the feasible geometric space into two regions:  $(\underline{F}_{K_1} > \underline{F}_{K_2})$  and  $(\underline{F}_{K_2} > \underline{F}_{K_1})$ . In the region  $(\underline{F}_{K_1} > \underline{F}_{K_2})$ , the lower boundary of  $F_{\max}$  is defined by  $\underline{F}_{K_1}$  and in the region  $(\underline{F}_{K_2} > \underline{F}_{K_1})$ , it is defined by  $\underline{F}_{K_2}$ .

From the expressions of  $\underline{F}_{K_1}$  and  $\underline{F}_{K_2}$  in [Eqs. \(18\)](#) and [\(21\)](#), it is observed that only one factor in the denominator is different between them. Hence, the condition for  $(\underline{F}_{K_1} > \underline{F}_{K_2})$  is obtained as:

$$c\eta - 2cs + s < c^3\eta - s^3 \quad (34)$$

$$\Rightarrow \eta < \eta_K, \text{ where, } \eta_K = \frac{2c - 1 - s^2}{cs} \quad (35)$$

Thus, within the feasible geometric space:

$$\text{Lower boundary of } F_{\max} = \max(\underline{F}_{K_1}, \underline{F}_{K_2}) = \begin{cases} \underline{F}_{K_1}, & \text{when } \eta < \eta_K \\ \underline{F}_{K_2}, & \text{when } \eta > \eta_K \end{cases} \quad (36)$$

The lower boundary as well as the upper boundary (i.e.,  $\bar{F}_k$ ) of  $F_{\max}$  can then be plotted as surfaces over the feasible geometric space  $(\eta, r)$ . The volume enclosed between these surfaces represents the feasible design space, i.e., the set of feasible  $(\eta, r, F_{\max})$  values for a given design problem. Note that any solution in this feasible space does define a complete design since the associated value of  $k$  can be obtained using [Eq. \(15\)](#).

### 4.4. Design strategy and numerical illustration for R-joint

All the derivations carried out in the previous sections have been consolidated into a flowchart with their corresponding equation numbers inside “()” in [Fig. 4](#), to present a global view of the process. In order to aid the understanding of this flowchart, some of its connections (marked in red color<sup>1</sup>) are explained in a step-wise manner.

- Firstly, all the conditions for design listed in [Table 1](#) are represented by the corresponding equation numbers [Eqs. \(11a\), ..., \(11g\)](#).
- Using the equality condition in [Eq. \(11b\)](#), one arrives at an expression for  $k$  in terms of  $(\eta, r, F_{\max})$  as shown in [Eq. \(15\)](#). It is noted that the entire expression could not be presented in the flowchart owing to the large expressions, nevertheless a functional form, such as  $k(\eta, r, F_{\max})$ , is indicated in such cases.
- Using the expression of  $k$  from [Eq. \(15\)](#), the inequality in [Eq. \(11c\)](#) can be reduced to a lower bound on  $F_{\max}$  (i.e.,  $F_{\max} \geq \underline{F}_{K_1}$ ) as shown in [Eq. \(18\)](#). Similarly, the condition  $k \leq \bar{k}$  from [Eq. \(11e\)](#) can be reduced to an upper bound on  $F_{\max}$  ( $F_{\max} \leq \bar{F}_k$ ) as in [Eq. \(23\)](#).
- In order to satisfy both the conditions  $F_{\max} \geq \underline{F}_{K_1}$  and  $F_{\max} \leq \bar{F}_k$ , it is necessary that  $\bar{F}_k \geq \underline{F}_{K_1}$ . This inequality results in three conditions represented in [Eqs. \(30\)–\(32\)](#). The first one is devoid of any design variables and hence imposes a necessary condition on the input parameters. The remaining conditions ([Eqs. \(31\)](#) and [\(32\)](#)) represent inequalities on the geometric variables,  $\eta > \underline{\eta}$  and  $r \geq r_{K_1}(\eta)$ , which must be considered for the computation of the feasible geometric space.

It is noted that all other connections in this flowchart have an analogous interpretation.

<sup>1</sup> The reader is referred to the web-version of this article for the interpretation of colors.

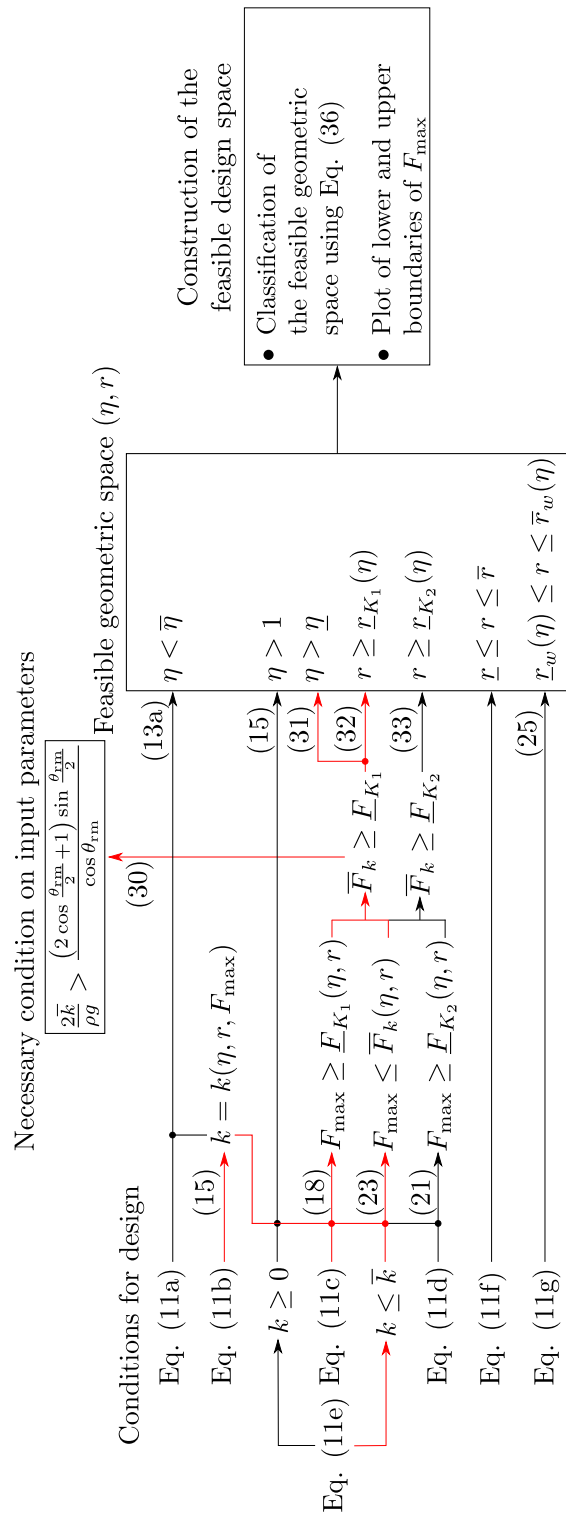


**Fig. 4.** Consolidation of all the conditions derived for obtaining the feasible design space for the R-joint. The respective equation numbers are denoted within parenthesis and the final results are highlighted in boxes.

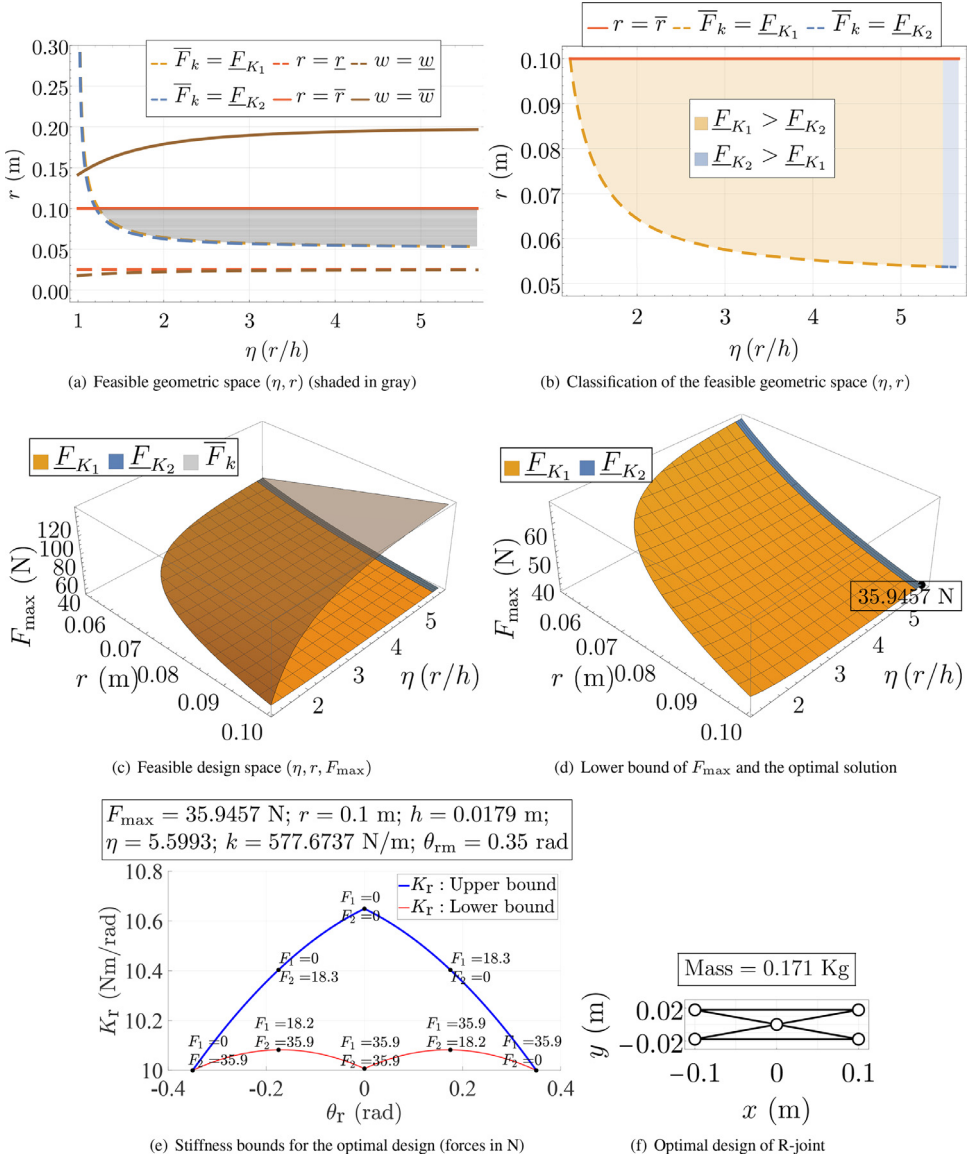


**Fig. 5.** Specification A: Feasible geometric and design spaces, stiffness bounds and schematic of the optimal design minimizing the maximal actuation force for the R-joint, when  $\theta_{rm} = 0.35$  radians ( $\approx 20^\circ$ ),  $\underline{K} = 10$  Nm/rad.

The final results that will be used directly in the design process, are consolidated into three boxes. The first one highlights the necessary condition that must be satisfied by the input parameters for the existence of feasible designs. The second box highlights the conditions that are needed to compute the feasible geometric space  $(\eta, r)$ . The last box shows the steps involved in the determination of the feasible design space.

As an illustration, consider the numerical example corresponding to specification A in Section 6, where  $\theta_{rm}$  is specified to be 0.35 radians, with a minimum desired stiffness,  $\underline{K} = 10$  Nm/rad. The mass and payload parameters are assumed to be:  $\rho = 0.2121$  Kg/m,  $M = 0.2$  Kg,  $d = 0.25$  m. The bounds on spring constant and link lengths are considered to be:  $(\underline{k}, \bar{k}) = (0, 2000)$  N/m,  $(\underline{r}, \bar{r}) = (0.025, 0.1)$  m, and  $(\underline{w}, \bar{w}) = (0.025, 0.2)$  m. Suppose that we wish to minimize the maximal actuation force  $F_{\max}$ . The optimal design is found from the following steps:

- The values of  $\cos \theta_{rm} = 0.9394$ ,  $\bar{\eta} = 5.6558$ ,  $P = \frac{2\bar{k}}{\rho g} = 1924.7763$ ,  $\underline{P}(\bar{\eta}) = \frac{(2c+1)s}{c^2-s^2} = 0.5504$ . Thus, the necessary condition  $P \geq \underline{P}(\bar{\eta})$ , is satisfied. From Eq. (31),  $\underline{\eta} = 1.0009$ .
- The feasible geometric space  $(\eta, r)$  is obtained by computing the intersection of the conditions in Eqs. (11f), (13a), (25), (31), (32), and (33), as shown in Fig. 5(a) (shaded in gray). The lower bounds on  $r$  are plotted in dashed lines, while the

upper bounds are plotted in continuous lines. It is observed that the feasible region is bounded by  $\eta = \bar{\eta}$ ,  $r = \bar{r}$ ,  $\bar{F}_k = F_{K_1}$ , and  $\bar{F}_k = F_{K_2}$ , in this case.

- From Eq. (35),  $\eta_K = 5.4777$ , which is less than  $\bar{\eta}$ . The classification of feasible geometric space is shown in Fig. 5(b), where the region ( $F_{K_1} > F_{K_2}$ ) is highlighted in orange shade, and the region ( $F_{K_2} > F_{K_1}$ ), in blue shade. The lower and upper bounds of  $F_{\max}$  are plotted over the feasible geometric space in Fig. 5(c). The volume enclosed between the surface  $\bar{F}_k$  (gray) and the surfaces  $F_{K_1}$  (orange),  $F_{K_2}$  (blue) defines the feasible design space  $(\eta, r, F_{\max})$  for the design problem at hand.
- From Fig. 5(d), it is observed that the optimal design corresponding to the least value of  $F_{\max}$  occurs when  $\eta = \bar{\eta}$  and  $r = \bar{r}$ . But, considering the condition  $\eta < \bar{\eta}$  (see Eq. (13a)), a factor  $\sigma = 0.99$  must be multiplied with  $\bar{\eta}$ , to remain close to the optimal solution while respecting the strict inequality on  $\eta$ . Therefore, the numerical values for optimal design of R-joint are found to be:  $\eta^*(\frac{r}{h}) = \sigma\bar{\eta} = 5.5993$ ,  $r^* = \bar{r} = 0.1$  m,  $F_{\max}^* = 35.9457$  N,  $k^* = 577.6737$  N/m. The stiffness bounds and a schematic representation of this design are shown in Figs. 5(e) and 5(f), respectively. From Fig. 5(e), it can be verified that the R-joint is able to reach the stipulated WFW:  $\theta_r \in [-0.35, 0.35]$  radians and the lower boundary of stiffness remains above the specified value of 10 Nm/rad, thereby validating the design requirements.

## 5. Complete feasible design space and design strategy for X-joint

As in the case of R-joint, a methodology for building the complete feasible design space is proposed for the X-joint in this section. The conditions on the right column of Table 1 are reduced to inequalities involving only  $(\lambda, b, F_{\max})$  in Section 5.1. The computation of feasible geometric space  $(\lambda, b)$  and of the feasible design space  $(\lambda, b, F_{\max})$  are carried out in Sections 5.2 and 5.3, respectively. Finally, a design strategy is presented for the X-joint with a numerical example in Section 5.4.

### 5.1. Treatment of the constraints involved in the design of X-joint

In the context of X-joint, the substitutions  $c = \cos\theta_{Xm}$ ,  $s = \sin\theta_{Xm}$ , and  $\lambda = \frac{l}{b}$ , have been incorporated for the ease of analysis. Since it is known that  $\theta_{Xm} \in [0, \frac{\pi}{2}]$ , it follows that  $c, s \in [0, 1]$ . The list of conditions in Eqs. (12b)–(12g) in Table 1 are treated successively in the following.

Using Eq. (8), the condition in Eq. (12b), expands into:

$$bcF_{\max} \left( \frac{s}{\sqrt{\lambda^2 - c^2}} - 1 \right) + \frac{C_2 s(2c^2 - \lambda^2)}{\sqrt{\lambda^2 - c^2}} + 2csC_1 = 0 \quad (37)$$

Solving for  $C_1$  from the above equation leads to:

$$C_1 = \frac{bcF_{\max}(\sqrt{\lambda^2 - c^2} - s) + C_2 s(\lambda^2 - 2c^2)}{2cs\sqrt{\lambda^2 - c^2}} \quad (38)$$

Using Eq. (38), all the inequalities in Table 1 for the X-joint can be reduced to conditions involving  $(\lambda, b, F_{\max})$ , as shown in the following.

- Condition on joint stiffness in Eq. (12c):

Using Eq. (10), the inequality in Eq. (12c) expands into:

$$2C_1 - \frac{C_2(\lambda^2 - 2)}{\sqrt{\lambda^2 - 1}} - K \geq 0 \quad (39)$$

Substituting for  $C_1$  from Eq. (38) results in:

$$\begin{aligned} & \left[ bcF_{\max}\sqrt{\lambda^2 - 1} \left( \sqrt{\lambda^2 - c^2} - s \right) + C_2 s \left\{ \sqrt{\lambda^2 - 1} (\lambda^2 - 2c^2) - c(\lambda^2 - 2)\sqrt{\lambda^2 - c^2} \right\} \right. \\ & \left. - Ksc\sqrt{\lambda^2 - 1}\sqrt{\lambda^2 - c^2} \right] / \left[ c\sqrt{\lambda^2 - 1}s\sqrt{\lambda^2 - c^2} \right] \geq 0 \end{aligned} \quad (40)$$

Recalling that  $\lambda > 1$ , it is apparent that  $(\sqrt{\lambda^2 - c^2} > s)$ . Thus, the denominator as well as the coefficient of  $F_{\max}$  in the numerator are both positive, which allows one to reduce the above inequality to a lower bound on  $F_{\max}$  as follows:

$$\begin{cases} F_{\max} \geq F_{K_1}, \text{ where} \\ F_{K_1} = \frac{Ksc\sqrt{\lambda^2 - 1}\sqrt{\lambda^2 - c^2} - C_2 s \left\{ \sqrt{\lambda^2 - 1} (\lambda^2 - 2c^2) - c(\lambda^2 - 2)\sqrt{\lambda^2 - c^2} \right\}}{bc\sqrt{\lambda^2 - 1}(\sqrt{\lambda^2 - c^2} - s)} \end{cases} \quad (41)$$

- Condition on joint stiffness in Eq. (12d):

Using Eq. (10), the inequality in Eq. (12d) can be expanded into:

$$bF_{\max} \left( \frac{\lambda^2(c^2 - s^2) - c^4}{(\lambda^2 - c^2)^{3/2}} + s \right) + 2C_1(c^2 - s^2) - \frac{cC_2 \left\{ (-c^2 + \lambda^2 + s^2)^2 - (\lambda^2 - 1)(c^2 - s^2) \right\}}{(\lambda^2 - c^2)^{3/2}} - K \geq 0 \quad (42)$$

Substituting for  $C_1$  from Eq. (38), leads to a lower bound on  $F_{\max}$ , similar to the previous case:

$$F_{\max} \geq F_{K_2}, \text{ where } F_{K_2} = \frac{c\underline{K}s(\lambda^2 - c^2)^{3/2} + C_2\lambda^4 s^3}{bc^3((\lambda^2 - c^2)^{3/2} - s^3)} \quad (43)$$

- Bounds on  $k$  in Eq. (12d):

Using the definition of  $C_1$  from Eq. (8) in Eq. (38), an expression for  $k$  can be obtained in terms of  $(\lambda, b, F_{\max})$  as follows:

$$k = \frac{bcF_{\max}(\sqrt{\lambda^2 - c^2} - s) + C_2 s(\lambda^2 - 2c^2) + 4cdgMs\sqrt{\lambda^2 - c^2}}{4b^2cs\sqrt{\lambda^2 - c^2}} \quad (44)$$

The lower and upper bounds on  $k$  lead to explicit conditions on  $F_{\max}$ , as derived below:

- Lower bound on  $k$  ( $k \geq 0$ ):

Substituting the expression of  $k$  from Eq. (44) in the condition  $k \geq 0$ , and observing that the denominator as well as the coefficient of  $F_{\max}$  are both positive, one obtains:

$$F_{\max} \geq F_k, \text{ where } F_k = \frac{-C_2 s(\lambda^2 - 2c^2) - 4cdgMs\sqrt{\lambda^2 - c^2}}{bc(\sqrt{\lambda^2 - c^2} - s)} \quad (45)$$

Since  $C_2 > 0$  by definition (see Eq. (8)), it is clear that  $F_k$  is negative when  $(\lambda^2 - 2c^2) > 0$ . Recalling that  $\lambda > 1$ , it is clear that the above inequality is always satisfied when  $(2c^2 < 1)$  or  $(c < \frac{1}{\sqrt{2}})$  or  $(\theta_{xm} > \frac{\pi}{4})$ . This implies that the condition  $k \geq 0$  remains satisfied when the design of X-joint is carried out for  $\theta_{xm} \geq 45^\circ$ , which is an interesting information. However, there exists a non-trivial lower bound for  $F_{\max}$  when  $\lambda^2 < 2c^2$ .

- Upper bound on  $k$  ( $k \leq \bar{k}$ ):

Substituting for  $k$  from Eq. (44) into  $(k - \bar{k} \leq 0)$  and simplifying leads to:

$$F_{\max} \leq \bar{F}_k, \text{ where } \bar{F}_k = \frac{4b^2\bar{c}ks\sqrt{\lambda^2 - c^2} - C_2 s(\lambda^2 - 2c^2) - 4cdgMs\sqrt{\lambda^2 - c^2}}{bc(\sqrt{\lambda^2 - c^2} - s)} \quad (46)$$

- Bounds on  $l$  in Eq. (12g):

From the definition of  $\lambda$ , it follows that:  $l = \lambda b$ . Substituting this expression for  $l$  into Eq. (12g) leads to:

$$\underline{l} \leq \lambda b \leq \bar{l} \Rightarrow \begin{cases} b \geq \underline{b}_l, \text{ where } \underline{b}_l = \frac{\underline{l}}{\lambda} \\ b \leq \bar{b}_l, \text{ where } \bar{b}_l = \frac{\bar{l}}{\lambda} \end{cases} \quad (47)$$

The bounds on  $l$  have resulted in inequalities involving only  $\lambda$  and  $b$ .

The conditions derived above will be used to determine the feasible geometric space  $(\lambda, b)$  and the bounds of  $F_{\max}$  inside this space, as detailed in the following.

## 5.2. Feasible geometric space $(\lambda, b)$ for X-joint

As in the case of R-joint, the design space is composed of only the two geometric variables  $(\lambda, b)$ , in addition to  $F_{\max}$ . Indeed,  $k$  can be expressed as a function of  $\lambda$  and  $b$  using Eq. (44). Determination of the feasible geometric space requires conditions:  $(\bar{F}_k \geq F_k)$ ,  $(\bar{F}_k \geq F_{K_1})$ , and  $(\bar{F}_k \geq F_{K_2})$ , to be satisfied along with the bounds on  $b$  and  $l$ . From Eqs. (45) and (46), it is observed that the expression of  $\bar{F}_k$  contains only an additional positive term,  $(4b^2\bar{c}ks\sqrt{\lambda^2 - c^2})$ , in its numerator when compared to that of  $F_k$ . This shows that the condition  $(\bar{F}_k \geq F_k)$  will always be satisfied without imposing any additional constraints on the design variables. Thus, the remaining two conditions involving bounds on  $F_{\max}$  are treated in the following.

### 5.2.1. Treatment of $(\bar{F}_k \geq F_{K_1})$

Substituting for  $F_{K_1}$  and  $\bar{F}_k$  from Eqs. (41) and (46), in the condition  $(\bar{F}_k - F_{K_1} \geq 0)$  yields:

$$\frac{s\sqrt{\lambda^2 - c^2} \left\{ -\sqrt{\lambda^2 - 1}(-4b^2\bar{k} + 4dgM + K) + C_2(-\lambda^2 + 2) \right\}}{b\sqrt{\lambda^2 - 1}(\sqrt{\lambda^2 - c^2} - s)} \geq 0 \quad (48)$$

It is observed that all factors but the second one in the numerator are positive. Thus, the preceding condition simplifies to:

$$-\sqrt{\lambda^2 - 1}(-4b^2\bar{k} + 4dgM + \underline{K}) + C_2(-\lambda^2 + 2) \geq 0 \quad (49)$$

Substituting for  $C_2$  from Eq. (8) into the above condition leads to the following inequality in  $b$ :

$$q_1(\lambda, b) := A_{b_1}b^2 + B_{b_1}b + C_{b_1} \geq 0, \text{ where,} \quad (50)$$

$$\begin{cases} A_{b_1} = 4\bar{k}\sqrt{\lambda^2 - 1} - g(\lambda + 1)(\lambda^2 - 2)\rho \\ B_{b_1} = -g(\lambda^2 - 2)M \\ C_{b_1} = -\sqrt{\lambda^2 - 1}(4dgM + \underline{K}) \end{cases} \quad (51)$$

From the expressions of the coefficients it is observed that ( $C_{b_1} < 0$ ), while the signs of the other two coefficients are dependent on  $\lambda$ . The roots of the quadratic expression are given by:

$$(b_1)_1 = \frac{-B_{b_1} - \sqrt{B_{b_1}^2 - 4A_{b_1}C_{b_1}}}{2A_{b_1}}, \text{ and } (b_2)_1 = \frac{-B_{b_1} + \sqrt{B_{b_1}^2 - 4A_{b_1}C_{b_1}}}{2A_{b_1}} \quad (52)$$

An interesting observation from Eq. (51) is that the coefficients are independent of  $\theta_{XM}$ , which implies that this constraint does not vary even if the design is performed for a different WFW specification. The signs of  $A_{b_1}$  and  $B_{b_1}$  are studied in a case-wise manner in the following:

- ( $\lambda^2 \leq 2$ ):

In this case,  $A_{b_1} > 0$ ,  $B_{b_1} \geq 0$ ,  $C_{b_1} < 0$ . From Appendix D, the solution to the inequality in Eq. (50) is given by:  $b \geq (b_2)_1$ .

- ( $\lambda^2 > 2$ ):

In this case,  $B_{b_1} < 0$ ,  $C_{b_1} < 0$ . Thus, in order to satisfy the inequality in Eq. (50), it becomes necessary to impose the condition:  $A_{b_1} > 0$ . Thus, following Appendix D, the solution in this case is also given by:  $b \geq (b_2)_1$ .

The condition ( $A_{b_1} > 0$ ), after squaring and simplifying, leads to:

$$p(\lambda) := (\lambda^6 + 2\lambda^5 - 3\lambda^4 - 8\lambda^3 + 8\lambda - \lambda^2P'^2 + P'^2 + 4) < 0 \quad (53)$$

where  $P' = \frac{4\bar{k}}{\rho g}$ . Unlike in the case of R-joint, explicit conditions on  $P'$  could not be derived for the X-joint. But, for a given value of  $P'$ , the feasible range of  $\lambda$  can be obtained, numerically. In summary, for  $(\bar{F}_k - F_{K_1}) \geq 0$  to be satisfied, the conditions  $p(\lambda) < 0$  and  $b \geq (b_2)_1$  must be considered together.

### 5.2.2. Treatment of $(\bar{F}_k \geq F_{K_2})$

Substituting for  $F_{K_2}$  and  $\bar{F}_k$  from Eqs. (43) and (46), in the condition  $(\bar{F}_k - F_{K_2} \geq 0)$  yields:

$$\frac{4b^2c\bar{k}s\sqrt{\lambda^2 - c^2} + C_2s(2c^2 - \lambda^2) - 4cdgMs\sqrt{\lambda^2 - c^2}}{bc(\sqrt{\lambda^2 - c^2} - s)} - \frac{c\underline{K}s(\lambda^2 - c^2)^{3/2} + C_2\lambda^4s^3}{bc^3((\lambda^2 - c^2)^{3/2} - s^3)} \geq 0 \quad (54)$$

Substituting for  $C_2$  from Eq. (8), obtaining a common denominator, and clearing all the positive factors, results in a quadratic inequality in  $b$  as follows:

$$q_2(\lambda, b) = A_{b_2}b^2 + B_{b_2}b + C_{b_2} \geq 0, \text{ where,} \quad (55)$$

$$\begin{cases} A_{b_2} = g(\lambda + 1)\rho\{-2c^6 - c^2\lambda^2(s\sqrt{\lambda^2 - c^2} + \lambda^2 + s^2) + c^4(2s\sqrt{\lambda^2 - c^2} + 3\lambda^2 + 2s^2) - \lambda^4s^2\} \\ \quad + \bar{k}\{4c^3(\lambda^2\sqrt{\lambda^2 - c^2} + s^2\sqrt{\lambda^2 - c^2} + \lambda^2s) - 4c^5(\sqrt{\lambda^2 - c^2} + s)\} \\ B_{b_2} = gM[-2c^6 - c^2\lambda^2\{s(\sqrt{\lambda^2 - c^2} + s) + \lambda^2\} + c^4\{2s(\sqrt{\lambda^2 - c^2} + s) + 3\lambda^2\} - \lambda^4s^2] \\ C_{b_2} = dgM\{4c^5(\sqrt{\lambda^2 - c^2} + s) - 4c^3(\lambda^2\sqrt{\lambda^2 - c^2} + s^2\sqrt{\lambda^2 - c^2} + \lambda^2s)\} - c\underline{K}(\lambda^2 - c^2)^{3/2} \end{cases} \quad (56)$$

The above expressions are quite complicated for reduction into explicit conditions on  $\lambda$  and  $b$ . Hence, further study must be conducted numerically, by studying the signs of  $(A_{b_2}, B_{b_2}, C_{b_2})$  inside the feasible range<sup>2</sup> of  $\lambda$ , given by  $\lambda \in [1, \frac{l}{b}]$ . The conditions in Appendix D must be used appropriately depending on the cases that are encountered (see Table D.2).

<sup>2</sup> The maximum value of  $\lambda$  is obtained to be  $(\frac{l}{b})$  by considering the bounds specified on  $l$  and  $b$ .

### 5.3. Bounds of $F_{\max}$ and the feasible design space for X-joint

There are three possible lower bounds for  $F_{\max}$  inside the feasible geometric space for the X-joint,  $(F_{K_1}, F_{K_2}, F_k)$ . For a given value of  $(\lambda, b)$  inside the feasible geometric space, the greatest of the three lower bounds defines the lower boundary of  $F_{\max}$ .

In order to classify the feasible geometric space, as in the case of the R-joint, the boundary curves corresponding to:  $(F_{K_1} = F_{K_2})$ ,  $(F_{K_1} = F_k)$ ,  $(F_{K_2} = F_k)$  must be plotted inside the design space.

Following a similar procedure as in [Section 5.2.2](#), the equations corresponding to above mentioned boundaries can be reduced to quadratic equations in  $b$ :

$$q_i(\lambda, b) := A_{b_i}b^2 + B_{b_i}b + C_{b_i} = 0, \quad (57)$$

where  $i = 3, 4, 5$  correspond to the cases  $(F_{K_1} = F_{K_2})$ ,  $(F_{K_1} = F_k)$ ,  $(F_{K_2} = F_k)$ , respectively. The expressions of each of these coefficients can be found in [Appendix E](#). The roots of the quadratic equations can be computed analytically as functions of  $\lambda$  and the complete solution in each case is obtained by considering the union of both roots.

These boundary curves may divide the feasible geometric space into several regions. The greatest of the three lower bounds of  $F_{\max}$  (i.e.,  $F_{K_1}$  or  $F_{K_2}$  or  $F_k$ ) can be identified in each of these regions, by evaluating them at any point inside that region. Using this information, the lower boundary of  $F_{\max}$  can be plotted.

Hence, the feasible design space  $(\lambda, b, F_{\max})$  can be obtained as the volume enclosed between the lower and upper boundaries of  $F_{\max}$ . For each solution in this space, the corresponding value of  $k$  can be obtained using [Eq. \(44\)](#).

### 5.4. Design strategy and numerical illustration for X-joint

As in the case of R-joint, the derivations carried out in the previous sections and the final results for the design of X-joint are consolidated into a flowchart in [Fig. 6](#). As an illustration, consider the numerical example in [Section 6](#) corresponding to specification A, where  $\theta_{XM}$  is specified to be 0.35 radians, with a minimum desired stiffness,  $K = 10$  Nm/rad. The mass and payload parameters are set to:  $\rho = 0.2121$  Kg/m,  $M = 0.2$  Kg,  $d = 0.25$  m. The bounds on spring constant and link lengths are chosen to be equivalent to that of R-joint (see [Section 4.4](#)) as follows:  $(\underline{k}, \bar{k}) = (0, 2000)$  N/m,  $(\underline{b}, \bar{b}) = (0.05, 0.2)$  m,  $(\underline{l}, \bar{l}) = (0.05, 0.4)$  m.

As for the R-joint, we suppose that we want to minimize the maximal actuation force  $F_{\max}$ . The optimal design for the X-joint is then obtained through the following steps:

- It is found that  $P' = \frac{4\bar{k}}{\rho g} = 3849.5527$ , and that the feasible range of  $\lambda$  corresponding to  $p(\lambda) < 0$  (see [Eq. \(53\)](#)) is  $\lambda \in ]1, 61.5591[$ , which is much larger than  $\lambda \in ]1, \frac{\bar{l}}{\bar{b}} (= 8)[$ .
- It is found that  $A_{b_2} > 0, C_{b_2} < 0$  (see [Eq. \(56\)](#)) inside  $\lambda \in ]1, \frac{\bar{l}}{\bar{b}}[$ . Thus,  $q_2(\lambda, b) > 0$  leads to a lower bound on  $b$  as shown in [Fig. 7\(a\)](#) (blue dotted line). The feasible geometric space (shaded in gray) that lies at the intersection of the conditions highlighted in the first box of [Fig. 6](#), is shown in [Fig. 7\(a\)](#). Analogous to the R-joint, the lower bounds on  $b$  are plotted in dashed lines, while the upper bounds are plotted in continuous lines. It is observed that the feasible geometric space for the X-joint is bounded only by the limits on  $l$  and  $b$ , in this example.
- The boundaries corresponding to  $(F_{K_1} = F_{K_2})$ ,  $(F_{K_1} = F_k)$ , and  $(F_{K_2} = F_k)$ , i.e., zero level sets of  $q_3, q_4, q_5$  were plotted in the design space. It was observed that the curves  $(q_4 = 0)$  and  $(q_5 = 0)$  did not intersect the feasible geometric space, while the curve  $(q_3 = 0)$  split it into two regions. By evaluating  $q_4$  and  $q_5$  at one point ( $\lambda = 2, b = 0.1$ ) inside the feasible geometric space, it was found that the entire region corresponds to:  $(F_{K_1} > F_k)$  and  $(F_{K_2} > F_k)$ . Similarly, the nature of the split regions was characterized by evaluating  $q_3$  at one point in each of those regions. The obtained result is depicted in [Fig. 7\(b\)](#), where the region  $(F_{K_1} > F_{K_2})$  is shown in orange shade, and the region  $(F_{K_2} > F_{K_1})$ , in blue shade. As a next step, the surfaces corresponding to the lower bounds ( $F_{K_1}$  (orange),  $F_{K_2}$  (blue)) and the upper bound ( $\bar{F}_k$  (gray)) of  $F_{\max}$  have been plotted over the feasible geometric space  $(\lambda, b)$  as shown in [Fig. 7\(c\)](#). The volume enclosed between these surfaces forms the feasible design space  $(\lambda, b, F_{\max})$  for this problem.
- From the plot of lower boundary of  $F_{\max}$  in [Fig. 7\(d\)](#), it is apparent that the optimal design solution that results in a minimum actuation force occurs at  $l = \bar{l}, b = \bar{b}$ . Thus, the corresponding joint parameters are found to be:  $(\lambda^*(\frac{l}{b}) = 2, b^* = \bar{b} = 0.2$  m,  $l^* = \bar{l} = 0.4$  m,  $F_{\max}^* = 21.0137$  N,  $k^* = 79.3788$  N/m). The stiffness bounds and a schematic representation of this design are presented in [Figs. 7\(e\) and 7\(f\)](#), respectively. From [Fig. 7\(e\)](#), it can be verified that the X-joint is able to reach the stipulated WFW:  $\theta_X \in [-0.35, 0.35]$  radians and the lower boundary of stiffness remains above the specified value of 10 Nm/rad, thereby validating the design requirements.

## 6. Numerical examples and comparison

A comparative study between the optimal designs of R- and X- joints are carried out with numerical examples in this section.

The links are considered to be made of Aluminum alloy with a circular cross-section of diameter equal to 0.01 m. Consequently, the linear mass density of the links ( $\rho$ ) is found to be 0.2121 Kg/m. Point mass ( $M$ ), mass offset ( $d$ ) are

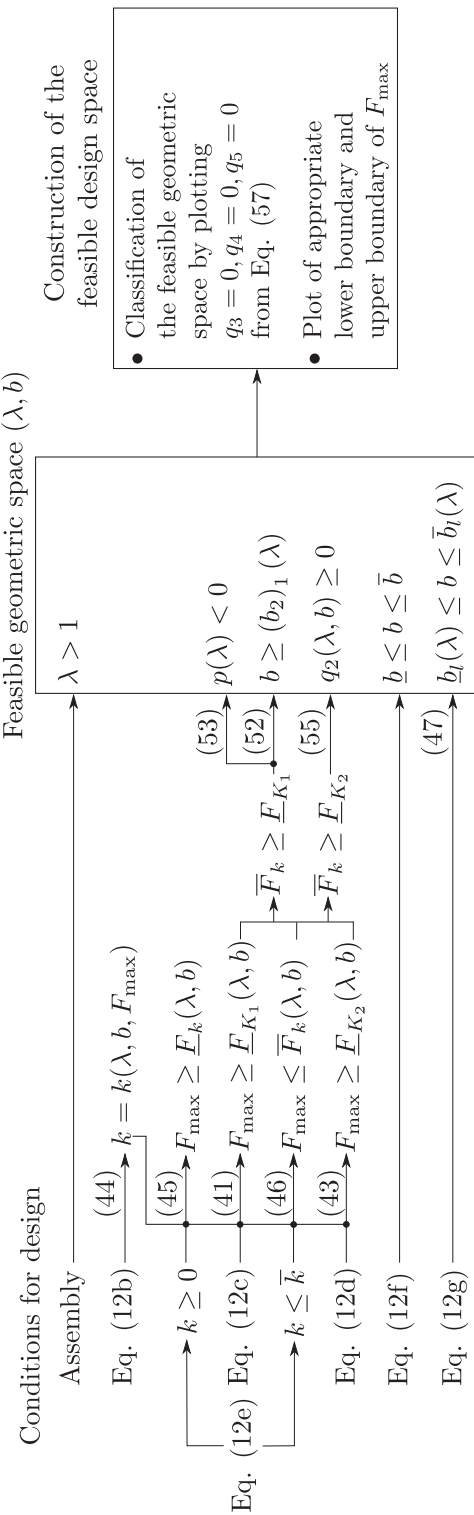


**Fig. 6.** Consolidation of all the conditions derived for obtaining the feasible design space for the X-joint. The respective equation numbers are denoted within parenthesis and the final results are highlighted in boxes.

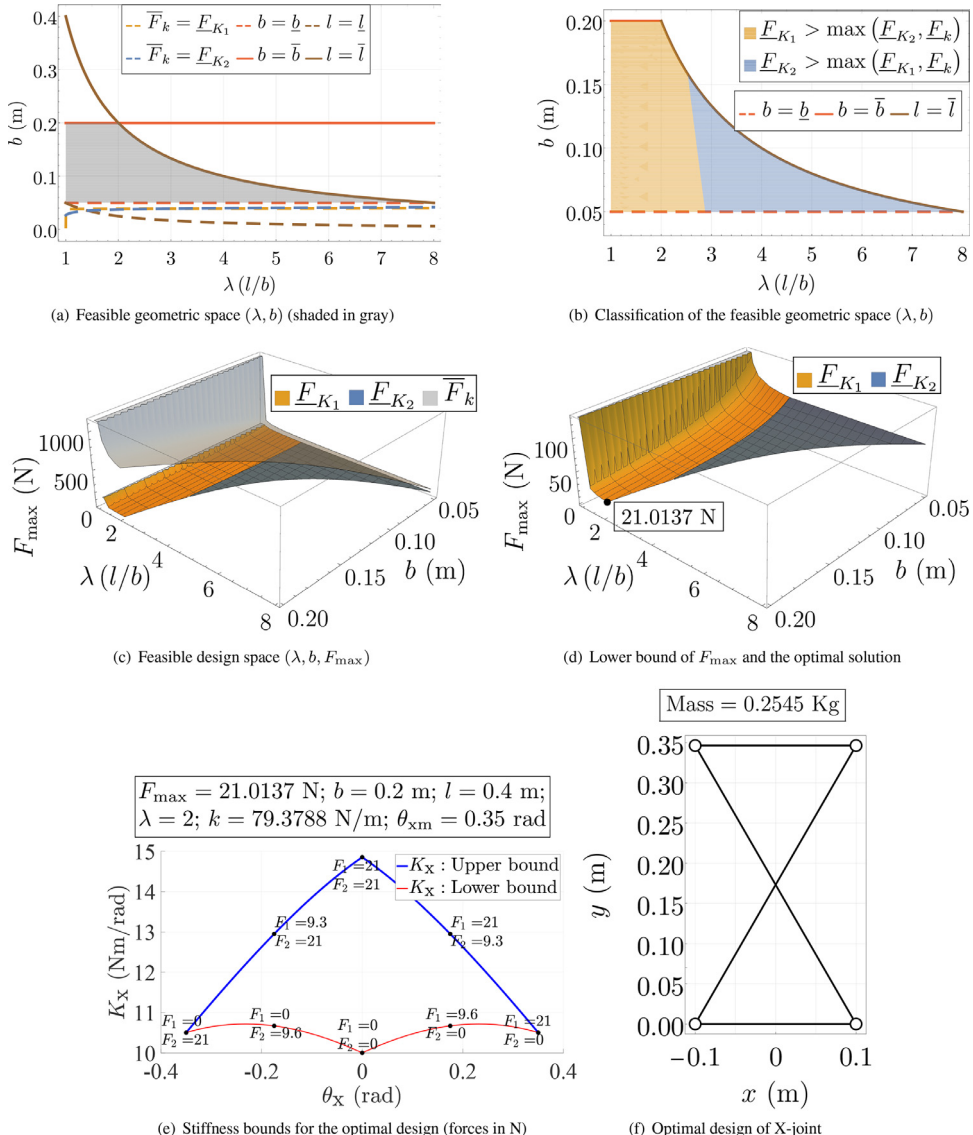


**Fig. 7.** Specification A: Feasible geometric and design spaces, stiffness bounds and schematic of the optimal design minimizing the maximal actuation force for the X-joint, when  $\theta_{xm} = 0.35$  radians ( $\approx 20^\circ$ ),  $K = 10$  Nm/rad.

set to:  $M = 0.2$  Kg and  $d = 0.25$  m. Four different specifications (A,B,C,D) for WFW have been considered:  $\theta_{rm} = \theta_{xm} = \{0.35, 0.7, 1.0, 1.3\}$  radians, respectively. Ideally, a suitable value for the minimum desired stiffness ( $K$ ) should be determined through experiments to estimate the amount of disturbance the joints must withstand. But, in this study these values are chosen, rather arbitrarily, to be 10 Nm/rad for specifications (A,B,C) and 1 Nm/rad for specification D. The value of  $K$  is reduced for the last specification because no feasible designs could be obtained with  $K = 10$  Nm/rad and  $\theta_{rm} = 1.3$  radians for the R-joint. Bounds on spring constant and link lengths are assumed to be:  $(k, \bar{k}) = (0, 2000)$  N/m for both the joints,  $(r, \bar{r}) = (0.025, 0.1)$  m,  $(w, \bar{w}) = (0.025, 0.2)$  m for the R-joint, and  $(\underline{b}, \bar{b}) = (0.05, 0.2)$  m,  $(\underline{l}, \bar{l}) = (0.05, 0.4)$  m for the X-joint. Two case studies are considered for the comparison of these joints in the following.

### 6.1. Minimization of the maximal actuation force $F_{\max}$

For the purpose of comparison, the designs are first optimized with the objective to minimize the maximal actuation force  $F_{\max}$ . Since the design specification A has already been dealt with in detail for the R-joint in Section 4.4 and for the X-joint in Section 5.4, only the remaining specifications are considered in the following. The feasible geometric and design spaces, stiffness bounds and schematics corresponding to the optimal design are presented for specification B in Figs. 8, 9, for specification C in Figs. 10–12, and for specification D in Figs. 13, 14, for both the joints. The optimal designs of these

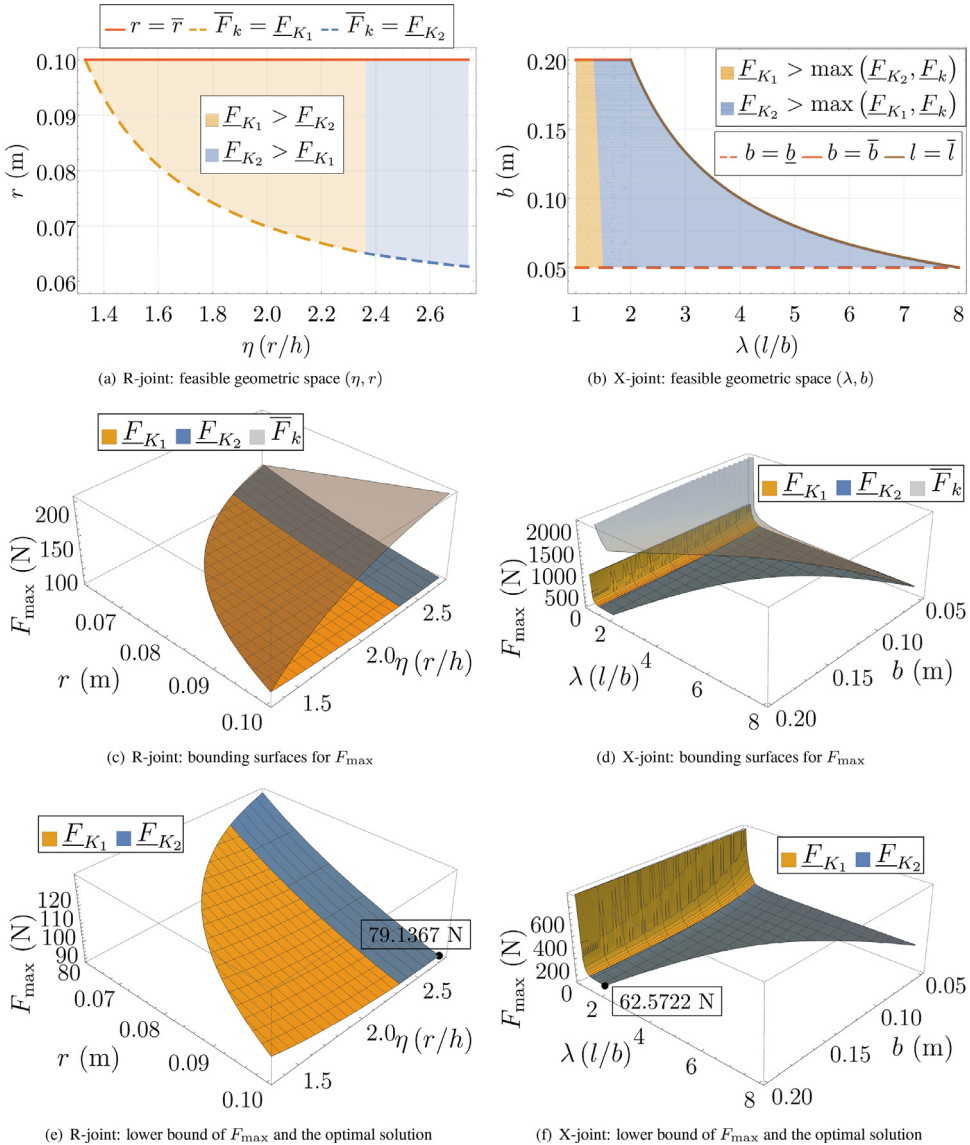


**Fig. 8.** Specification B: Feasible geometric space and bounding surfaces of  $F_{\max}$  for both R-joint and X-joint, when  $\theta_{rm} = \theta_{xm} = 0.7$  radians ( $\approx 40^\circ$ ),  $K = 10$  Nm/rad.

joints are compared in terms of their geometry, mass, springs, actuation forces, and stiffness. In general, it was observed that the R-joint tends to be shorter, requires much stronger springs, and possesses a more uniform distribution of stiffness throughout the WFW. In contrast, the X-joint achieves a much larger value of stiffness near the zero orientation and exhibits relatively large variations in stiffness within its WFW. In comparison with X-joint, the R-joint requires larger forces for small WFW specifications and much smaller forces for large WFW specifications. More specific details on the difference between the two joints are presented in the following.

- From the plots of the bounding surfaces of  $F_{\max}$ , it is observed that the range of  $F_{\max}$  as well as  $\lambda$  for the X-joint is much larger than the corresponding ranges of  $F_{\max}$  and  $\eta$  for the R-joint. This indicates that there are more feasible designs for X-joint satisfying the equivalent set of constraints.
- For both R- and X- joints, the region corresponding to ( $F_{K_2} > F_{K_1}$ ), i.e., the blue region, keeps increasing with the size of the WFW. This implies that the fraction of designs possessing the minimum stiffness ( $K$ ) at the boundary of WFW (instead of at the zero orientation) increases for both the joints with increase in WFW specification. Beyond  $\theta_{rm} = \theta_{xm} = 1.0$  radians, it is observed that the feasible geometric space only consists of the region ( $F_{K_2} > F_{K_1}$ ), for both the joints.

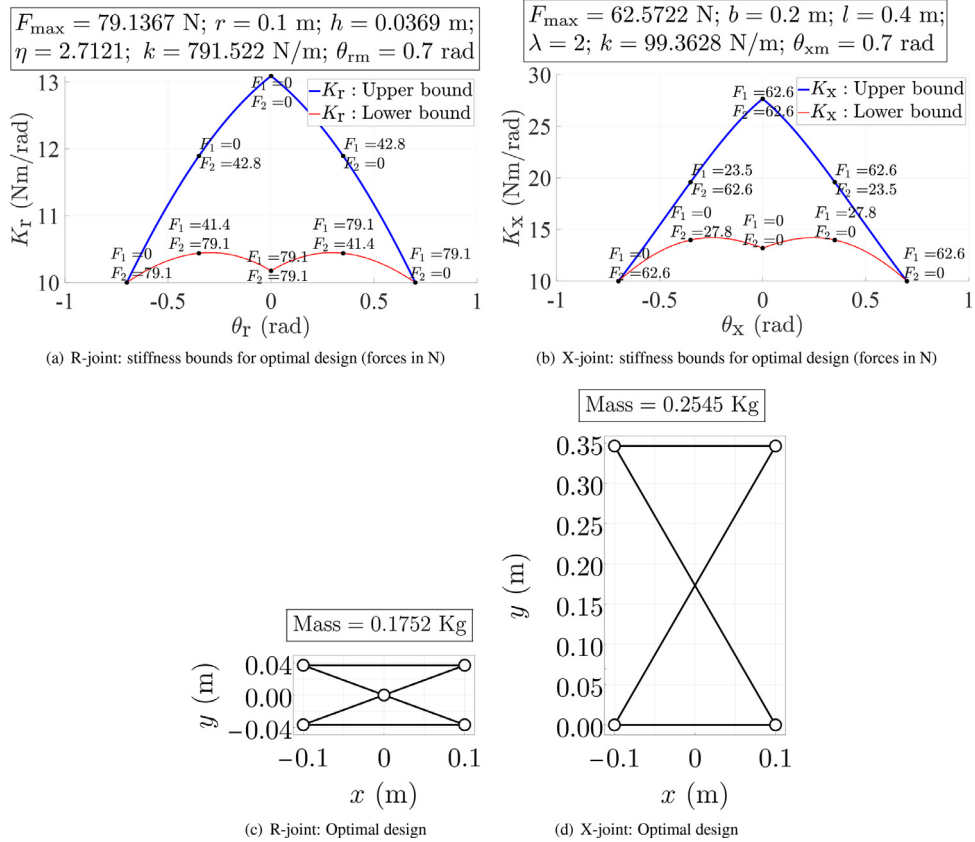


**Fig. 9.** Specification B: Stiffness bounds and schematics of the optimal design corresponding to minimum  $F_{\max}$ , for both R-joint and X-joint, when  $\theta_{rm} = \theta_{xm} = 0.7$  radians ( $\approx 40^\circ$ ),  $K = 10 \text{ Nm/rad}$ .

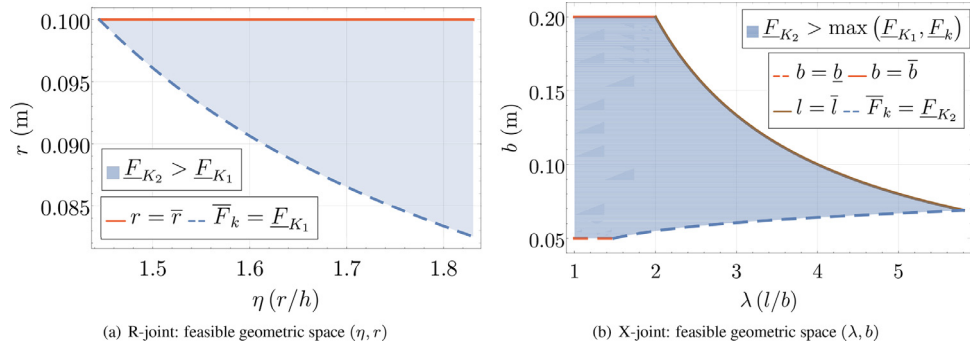


**Fig. 10.** Specification C: Feasible geometric space for both R-joint and X-joint, when  $\theta_{rm} = \theta_{xm} = 1.0$  radian ( $\approx 58^\circ$ ),  $K = 10 \text{ Nm/rad}$ .

- In all the examples, optimal design of R-joint occurs at  $r = \bar{r}$  and when  $\eta$  approaches its upper bound  $\bar{\eta}$ . Recalling that  $(\eta = \frac{r}{h})$ , a larger value for  $\eta$  implies that the R-joint tends to be shorter. On the other hand, for the X-joint, the optimal design occurs at  $b = \bar{b}$  and  $l = \bar{l}$  for three of the design specifications (A,B,C). This shows that the X-joint, in contrast to the R-joint, tends to be as large as possible in these cases. It is interesting to note that the specifications (A,B,C) yield the same geometry  $(b, l)$  and different spring constants for the X-joint. While, for the R-joint, three different geometries as well as spring constants are obtained for those specifications.
- The optimal value of force required is greater for the R-joint for specifications A (1.71 times) and B (1.26 times). On the other hand, the force required is significantly lower for the R-joint for specifications C (0.73 times) and D (0.07 times). Thus, when actuation force is the only criterion, the X-joint would be preferred for applications requiring only a small WFW (up to  $\theta_{\max} = 0.7$  radians), while R-joint would be favored for a relatively large WFW (beyond  $\theta_{\max} = 1$  radian).

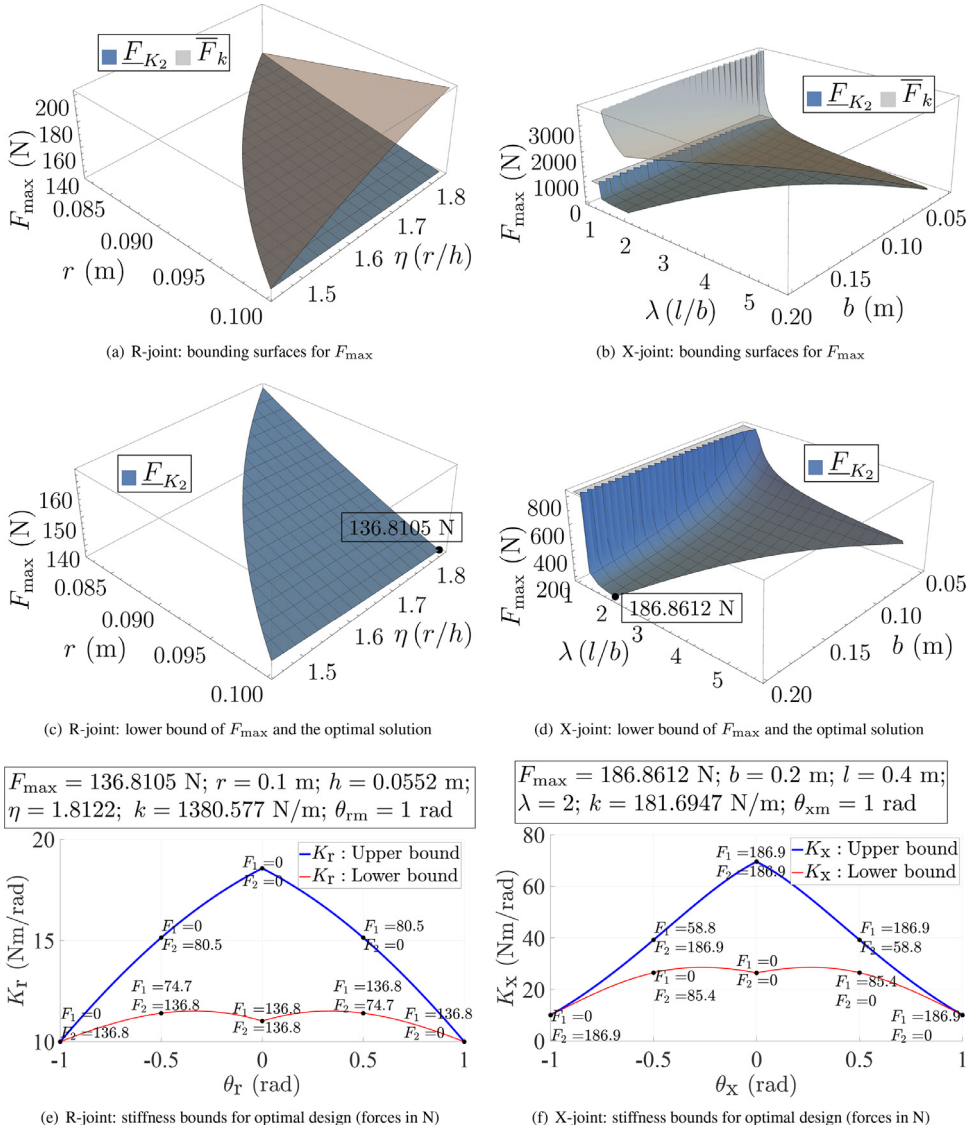


**Fig. 11.** Specification C: Bounding surfaces of  $F_{\max}$ , stiffness bounds of the optimal design corresponding to minimum  $F_{\max}$ , for both R-joint and X-joint, when  $\theta_{rm} = \theta_{xm} = 1.0$  radian ( $\approx 58^\circ$ ),  $\underline{K} = 10$  Nm/rad.

- For the X-joint,  $F_{\max}$  has turned out to be significantly larger for specification D ( $\theta_{xm} = 1.3$  radians,  $\underline{K} = 1$  Nm/rad), than specification C ( $\theta_{xm} = 1$  radian,  $\underline{K} = 10$  Nm/rad), despite a small increase in WFW and a much smaller stiffness specification. This is because in specification D, WFW boundary of the X-joint is very close to the flat singularity at  $\theta_x = \pm\frac{\pi}{2}$ . The stiffness value drops drastically near singularities, thereby, necessitating sufficiently large forces to counter the ill effects of such configurations. In order to study only the effect of large WFW requirement, a new specification D' (with  $\theta_{xm} = 1.3$  radians and  $\underline{K} = 10$  Nm/rad), which has the same  $\underline{K}$  as that of specification C, is considered. The corresponding optimal design is found to be:  $l = 0.4$  m,  $b = 0.2$  m,  $F_{\max} = 1108.6682$  N,  $k = 780.4586$  N/m. This shows that the X-joint requires roughly 3 times stronger springs and 3 times larger forces, for an increase in WFW from  $\theta_{xm} = 1$  radian to  $\theta_{xm} = 1.3$  radians, when  $\underline{K}$  is fixed at 10 Nm/rad.
- From the plot of stiffness bounds, it is observed that the maximum value of stiffness as well as its distribution are much larger for the X-joint when compared to its counterpart. Thus, for specifications A and B, the X-joint allows for a larger range of stiffness tuning, while requiring lower forces, which is a two-fold advantage over the R-joint for small WFW specifications. On the other hand, the R-joint can achieve a better stiffness resolution within the WFW, since a large range of forces map to a small range of stiffness for this joint.
- For all design specifications, the mass of the X-joint is slightly greater (about 1.02 – 1.49 times), while the value of spring constant is much lower (about 0.1 – 0.5 times), than the respective values of the R-joint. This shows that the R-joint is

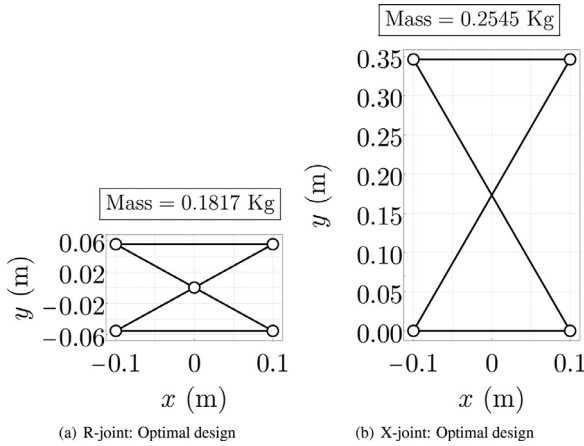


**Fig. 12.** Specification C: Schematic of the optimal design corresponding to minimum  $F_{\max}$  for both R-joint and X-joint, when  $\theta_{rm} = \theta_{xm} = 1.0$  radian ( $\approx 58^\circ$ ),  $K = 10$  Nm/rad.

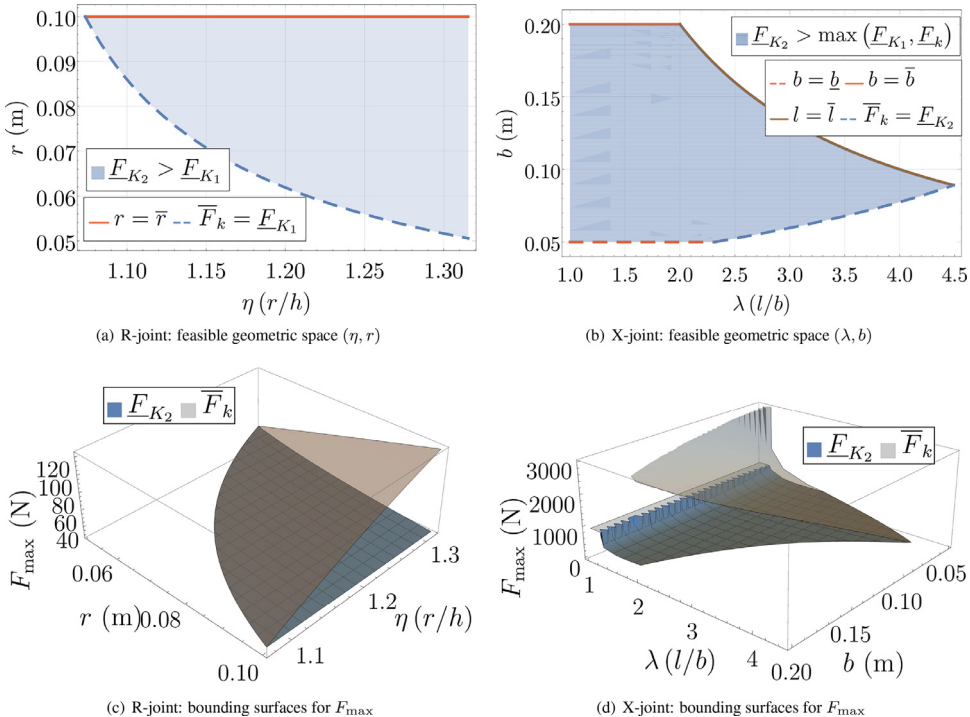


**Fig. 13.** Specification D: Feasible geometric space and bounding surfaces for  $F_{\max}$  for both R-joint and X-joint, when  $\theta_{rm} = \theta_{xm} = 1.3$  radians ( $\approx 75^\circ$ ),  $K = 1$  Nm/rad.

slightly lighter, but requires much stronger springs to achieve the same WFW and stiffness performance as that of the X-joint.

- In the design process, it is also imperative to verify if the optimal designs can withstand the forces they are subjected to during their operation, without failure. Since it is known that all the bars are loaded axially (mostly in compression), the buckling mode of failure seems the most susceptible. For the data presented above, the critical buckling load (see, e.g., [28], p. 819) of the longest possible Aluminum bar (upper bound  $\bar{l} = 0.4$  m) is computed to be 2119.5697 N. As an example, the optimal X-joint for specification D' (fifth bullet point) is considered since it has both the maximum force requirement and the longest bar among all the optimal designs. A safe overestimate of the compression load experienced by a crossed bar can be computed as:  $\{F_{\max} + k(l+b) + Mg\}$ , assuming maximum loading from the actuator, maximum permissible extension in the springs (flat configuration), and direct transmission of the payload weight. Substituting the corresponding joint parameters one obtains this load to be 1578.9034 N. Clearly, the overestimated compression load is

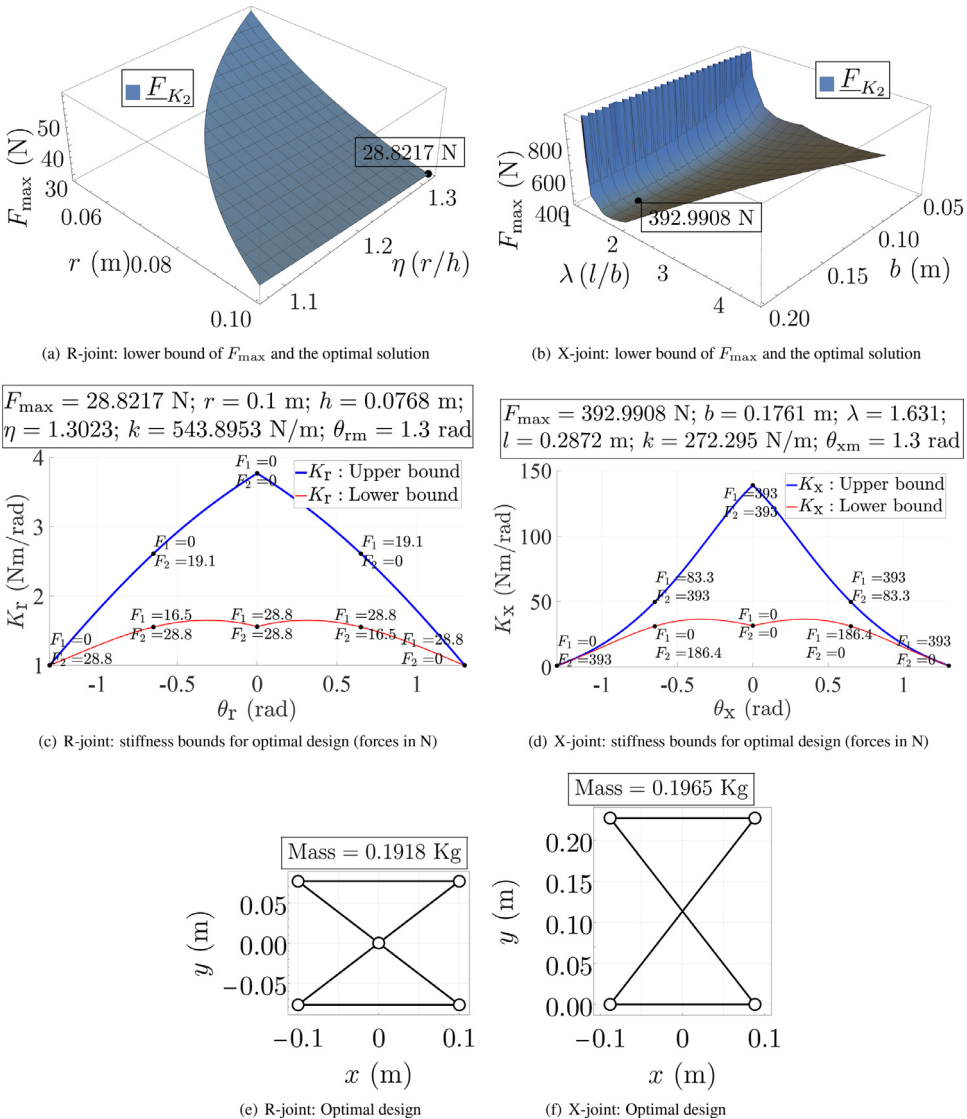


**Fig. 14.** Specification D: Lower bounding surface for  $F_{\max}$ , stiffness bounds and schematic of the optimal design corresponding to minimum  $F_{\max}$ , for both R-joint and X-joint, when  $\theta_{rm} = \theta_{xm} = 1.3$  radians ( $\approx 75^\circ$ ),  $K = 1$  Nm/rad.

less than the critical buckling load, thereby proving that this design is safe. Since all the other optimal designs of R- and X- joints are subject to much lesser actuation forces, they are also determined to be safe.

## 6.2. Minimization of the joint mass for a given $F_{\max}$

Since the tensegrity joints are suitable candidates for building lightweight manipulators, minimization of their mass is another criterion that can be of interest in the design process. In this scenario, the actuators are assumed to be available *a priori*, i.e.,  $F_{\max} = F_{\max}^0$  is a known quantity which is equal for both the joints. Practically, this corresponds to a situation where the designer wants to achieve the stipulated static performance (WFW and minimum stiffness) with the joints by varying their geometry and springs, while keeping them as light as possible. The comparison analysis is conducted between the optimal designs of R- and X- joints corresponding to minimum mass.

The feasible design space for this problem is defined by the intersection of the feasible design space derived previously and the plane  $F_{\max} = F_{\max}^0$  as shown in Fig. 15(a) (bounded by the dashed lines). The variation of joint mass can be plotted inside this feasible space and the optimal design can be identified directly, as in the previous scenarios. The maximal actuation forces have been fixed at  $F_{\max}^0 = 50$  N for specification A,  $F_{\max}^0 = 100$  N for specification B, and  $F_{\max}^0 = 190$  N for specification C. The specification D has not been considered since there exists no common  $F_{\max}^0$  ensuring feasible designs for

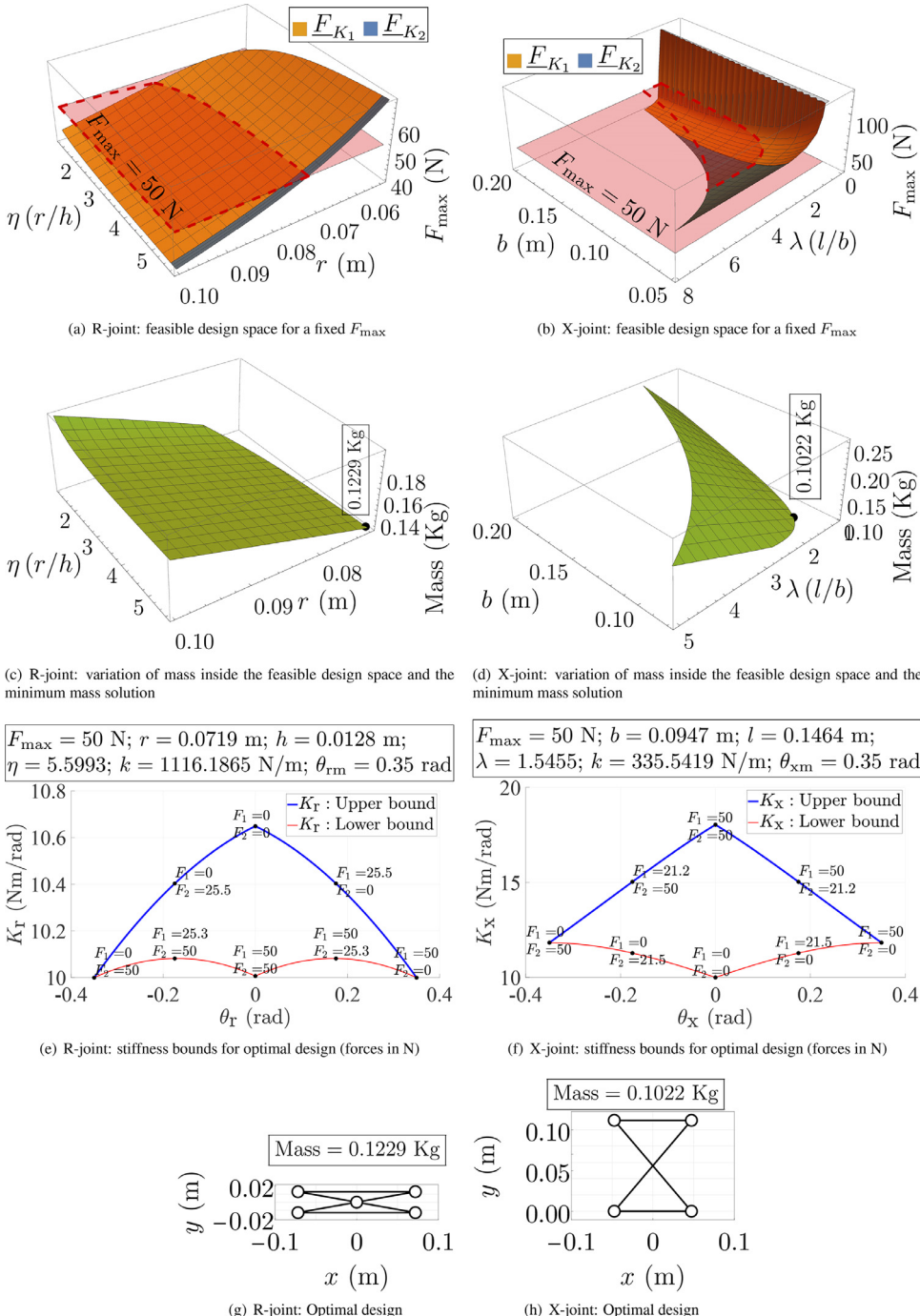


**Fig. 15.** Specification A: Feasible design space, variation of joint mass, stiffness bounds and schematic of the optimal design corresponding to minimum mass, for both R-joint and X-joint, when  $F_{\max} = 50 \text{ N}$ ,  $\theta_{rm} = \theta_{xm} = 0.35 \text{ radians } (\approx 20^\circ)$ ,  $K = 10 \text{ Nm/rad}$ .

both the joints, as explained in the following. The feasible design spaces, variation of masses, stiffness bounds and schematics of the optimal designs are shown for the two joints, for specification A in Fig. 15, B in Fig. 16, C in Figs. 17 and 18. The following observations are made from these plots.

- The value of  $F_{\max}^0$  has been chosen such that there exists a non-empty feasible design space for both the joints. However, such a choice does not exist for specification D as can be reasoned from the plots of feasible design spaces in Figs. 13(c) and (d). It is found that there exists no feasible designs for the R-joint when  $F_{\max} > 120 \text{ N}$ , and for the X-joint

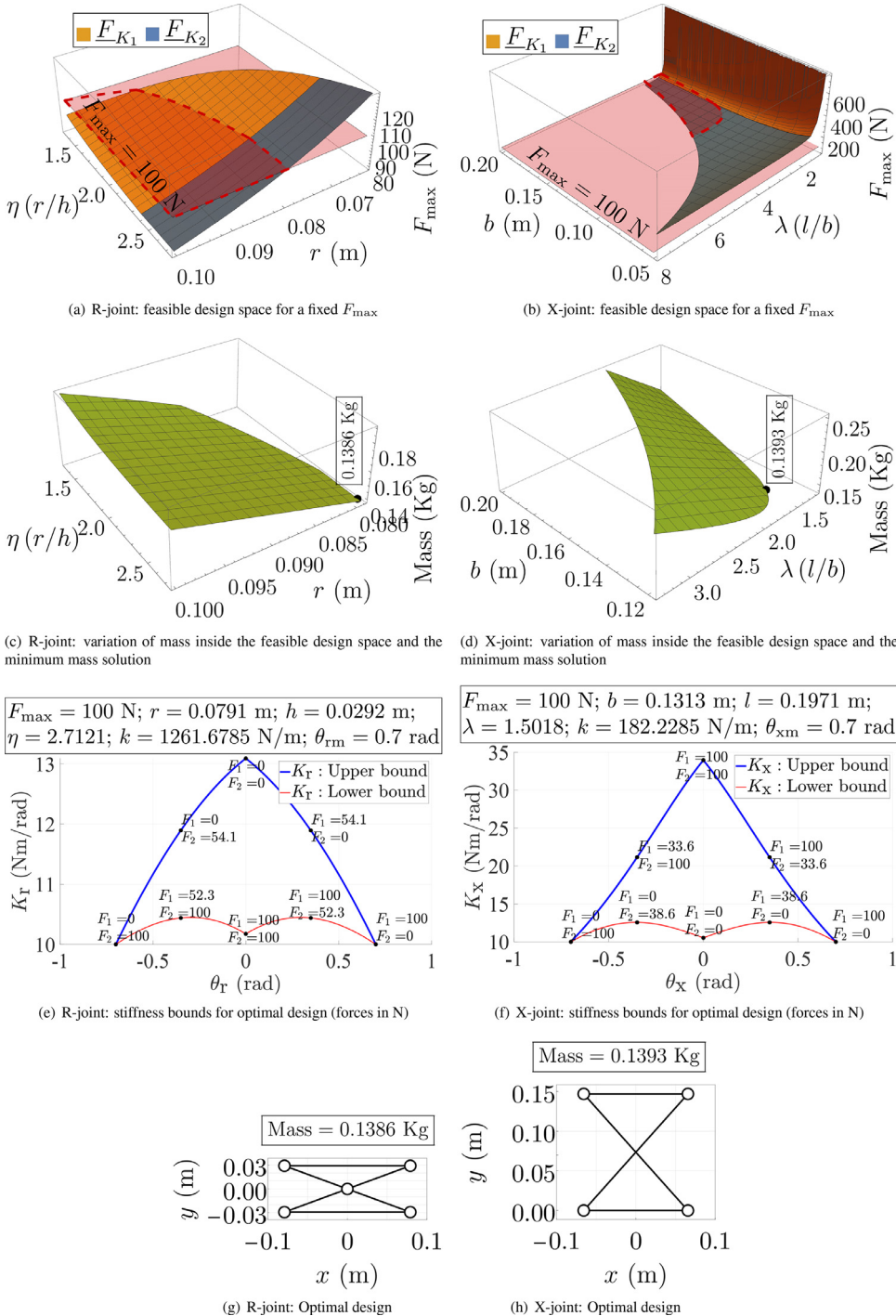


**Fig. 16.** Specification B: Feasible design space, variation of joint mass, stiffness bounds and schematic of the optimal design corresponding to minimum mass, for both R-joint and X-joint, when  $F_{\max} = 100 \text{ N}$ ,  $\theta_{rm} = \theta_{xm} = 0.7 \text{ radians}$  ( $\approx 40^\circ$ ),  $K = 10 \text{ Nm/rad}$ .

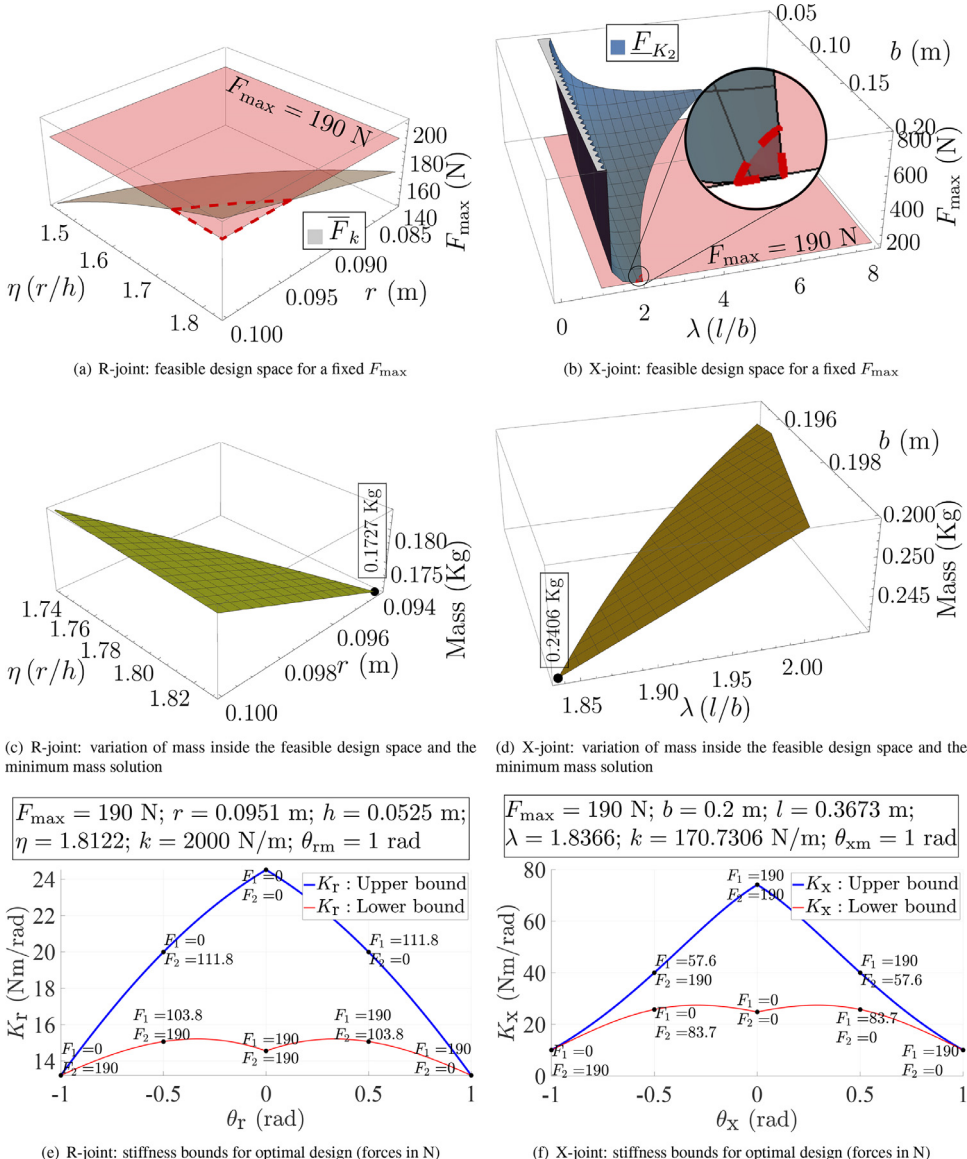


**Fig. 17.** Specification C: Feasible design space, variation of joint mass, stiffness bounds of the optimal design corresponding to minimum mass, for both R-joint and X-joint, when  $F_{\max} = 190$  N,  $\theta_{rm} = \theta_{xm} = 1$  radian ( $\approx 58^\circ$ ),  $K = 10$  Nm/rad.

when  $F_{\max} < 392$  N. Thus, it can be concluded that when the actuators are not strong enough to produce  $F_{\max} > 120$  N, only the R-joint can satisfy the stipulated requirements on stiffness for  $\theta_{\max} = 1.3$  radians.

- Recalling that the actuators are fixed at the base, the mass of R-joint is computed to be  $4\rho(r + w)$  (see Fig. 1(a), which can be rewritten in terms of the geometric variables as:

$$\text{Mass of R-joint} = 4\rho r \left( 1 + \sqrt{1 + \frac{1}{\eta^2}} \right), \text{ recalling } \eta = \frac{r}{h} \quad (58)$$

From the above expression, it is clear that the minimum mass solution requires  $r$  to be as small as possible and  $\eta$  to be as large as possible. From Figs. 15(a), 16(a) and 17(a), it is apparent that the smallest  $r$  for a given  $\eta$  occurs at the intersection of  $F_{\max} = F_{\max}^0$  and the lower/upper boundary of  $F_{\max}$ . Thus, the optimal solution must occur at the intersection of those surfaces and  $\eta = \bar{\eta}$  in all the examples. Plots in Figs. 15(c), 16(c), 17(c) confirm this result. As explained in Section 4.4,  $\eta = \sigma \bar{\eta}$ ,  $\sigma = 0.99$  must be considered in accordance with the strict inequality  $\eta < \bar{\eta}$ .

- Recalling that the actuators are fixed at the base, the mass of X-joint is given by  $2\rho(b + l)$  (see Fig. 1(b)) which can be rewritten as  $2\rho b(1 + \lambda)$ , recalling  $\lambda = \frac{l}{b}$ . This suggests that the mass of X-joint would be a minimum when  $b$  and  $\lambda$  are both as small as possible. From the plots of feasible design spaces in Figs. 15(b), 16(b), 17(b), it is found that  $\lambda$  and  $b$  are

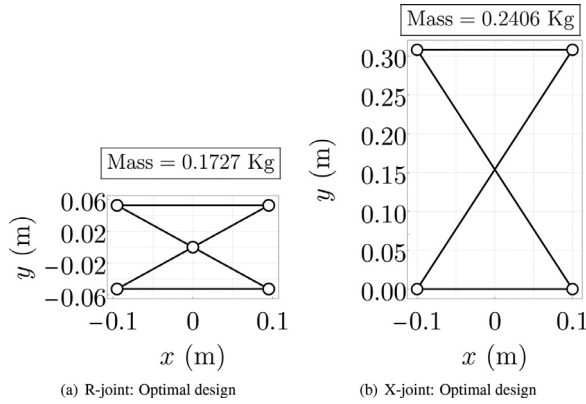


**Fig. 18.** Specification C: Schematic of the optimal design corresponding to minimum mass, for both R-joint and X-joint, when  $F_{\max} = 190$  N,  $\theta_{rm} = \theta_{xm} = 1$  radian ( $\approx 58^\circ$ ),  $K = 10$  Nm/rad.

conflicting objectives when minimized. The curve representing the trade-off between them is formed by the intersection of  $F_{\max} = F_{\max}^0$  and the lower boundary of  $F_{\max}$ . Thus, the minimum mass solution must occur on this curve, which can be solved for numerically by studying the variation of joint mass on it (see Figs. 15(d), 16(d), 17(d)).

- The width of the R-joint is greater (1.2 – 1.5 times) for specifications A and B, and is about equal for specification C, but the height of X-joint is significantly greater (2.4 – 4.4 times) in all the examples. In terms of mass, the R-joint is found to be slightly heavier (1.2 times) for specification A, about equal for specification B, and lighter (0.72 times) for specification C. Thus, when the same actuators are used for the two joints, the X-joint would be preferred for small WFW requirements (up to  $\theta_{\max} = 0.7$  radians), but the R-joint would be favored for larger WFW requirements, when joint mass is the criterion.
- The value of spring constant is found to be much higher (about 3 – 12 times) for the R-joint in these examples. In particular, for specification C the spring constant is equal to its upper bound of  $\bar{k} = 2000$  N/m for the R-joint, due to the occurrence of the optimal solution on the upper bound of  $F_{\max}$  ( $\bar{F}_k$ ).

The comments made on the stiffness bounds in the previous case study, are applicable to this problem as well.

## 7. Effect of mass density and payload

The influence of mass and payload parameters ( $\rho, M, d$ ) on the optimal design of the two joints was studied with several numerical examples. The patterns observed are summarized below:

- Influence of  $(\rho, M, d)$  on the optimal design of R-joint:

It is observed that increasing the values of  $(\rho, M, d)$ , roughly up to 5 times their original values, does not impact the geometry ( $r, \eta$ ) and the optimal force ( $F_{\max}$ ). This is because the lower boundaries of  $F_{\max}$  ( $\underline{F}_{K_1}, \underline{F}_{K_2}$ ), where the optimal design corresponding to minimum force occurs, are independent of  $(\rho, M, d)$  (see Eqs. (18) and (21)). However, spring constant  $k$  must change appropriately to compensate for the variations in mass/payload according to Eq. (15).

Nevertheless, the parameters  $(\rho, M, d)$  affect the size of the feasible design space (through curves ( $\bar{F}_k = \underline{F}_{K_1}$ ), ( $\bar{F}_k = \underline{F}_{K_2}$ )), and for relatively large increase (such as 10 times the default values) of these parameters, no feasible designs can be found for the R-joint.

- Influence of  $(\rho, M, d)$  on the optimal design of X-joint:

It is found that the parameters  $(\rho, M)$  directly influence two<sup>3</sup> of the lower boundaries of  $F_{\max}$  ( $\underline{F}_{K_1}, \underline{F}_{K_2}$ ) and hence the optimal value of force for the X-joint. On the other hand, the payload offset  $d$  affects only the size of the feasible design space and the existence of feasible designs, as in the case of R-joint. From numerical examples, it is observed that increasing  $(\rho, M)$  results in an increase of the optimal force  $F_{\max}$  required for the X-joint.

The maximal actuation forces required for the R-joint remains greater (resp. lower) than that of the X-joint for specifications A and B (resp. specifications C and D), even when the joint parameters  $(\rho, M, d)$  are significantly altered. Similarly, the minimum joint mass (when maximal actuation forces are fixed) for R-joint remains greater for specification A, about equal for specification B, and lesser for specification C in these experiments.

<sup>3</sup> The third lower boundary  $\underline{F}_k$  is not considered as it was never found to be greater than  $\underline{F}_{K_1}$  and  $\underline{F}_{K_2}$  to form the lower boundary of  $F_{\max}$  in any of the examples.

## 8. Effect of non-zero spring free-length

If a non-zero free-length is considered for the springs, then the following changes are observed in the WFW and stiffness of the joints:

- Impact on R-joint:

The size of the WFW logically decreases since the space occupied by the spring free-length reduces the rotation range. On the other hand, the stiffness increases irrespective of its geometry ( $r, h$ ). In some examples, it was found that  $l_1, l_2$  (see Fig. 1(a)) need to be smaller than the free-length of the springs to reach the boundary of the WFW, which is not permissible physically. Hence, as an extension of this work, it is planned to account for the free-length of springs in the design process itself with additional constraints for the R-joint.

- Impact on X-joint:

Unlike in the case of R-joint, it is observed that the size of the WFW increases for the X-joint when the spring free-length is non-zero, and the corresponding stiffness of the joint decreases. Moreover, if the spring free-length is chosen to be less than  $(l - b)$ , i.e., the spring lengths  $l_1, l_2$  (see Fig. 1(b)) at the flat singularities, then the springs continue to operate in the tension mode without any issues. Thus, no major changes would be necessary in the design process for the X-joint.

## 9. Conclusion

Two antagonistically actuated tensegrity joints, a revolute (R) joint and an anti-parallelogram (X) joint, have been analyzed and compared in this work. Design strategies have been proposed for these joints to possess a prescribed WFW with a minimum specified stiffness throughout. The strength of our approach lies in the complete characterization of the design space. This strategy requires some preliminary tedious algebraic calculations, but all feasible designs are obtained. This allows for selecting different optimal designs, such as, for instance, the ones with minimum actuation force or with minimal mass. The optimal designs of the two joints have been compared on the basis of actuation forces, stiffness, and geometry, while they were designed to possess the same WFW. It was observed that when the WFW range is smaller than  $[-0.7, 0.7]$  radians, the actuation force required for the R-joint is greater than that of the X-joint. On the other hand, when the WFW specification is larger than  $[-1, 1]$  radians, the force required for the X-joint is much greater due to its proximity to the flat singularity. While minimizing the joint masses for a fixed maximal actuation force, the R-joint turned out to be heavier when the WFW range is smaller than  $[-0.7, 0.7]$  radians, but lighter for larger WFW specifications. These observations on actuation forces and joint masses are found to be valid even when the mass density and payload parameters are significantly altered.

In general, the R-joint is shorter, requires much stronger springs, and possesses a more uniform distribution of stiffness throughout the WFW. On the other hand, the X-joint achieves a much larger value of stiffness near the zero orientation and exhibits relatively large variations in stiffness within its WFW. It is possible to increase the stiffness of the X-joint at any orientation by suitably increasing the actuation forces, but, this is not possible for the R-joint due to the negative influence of the actuation forces on stiffness.

In the future, robot manipulators with some or all of its joints replaced with the proposed tensegrity joints will be studied and experiments will be conducted on test beds.

### Declaration of Competing Interest

This is to declare that the authors of our manuscript have no conflict of interest.

### Acknowledgments

This work was conducted with the support of the French National Research Agency (AVINECK Project ANR-16-CE33-0025).

### Appendix A. Nature of lower bound of stiffness for R-joint

In this appendix, it is established formally that the actuation forces have a *negative* impact on the stiffness of the R-joint. Additionally, it is also shown that the least value of stiffness, when it is imposed to be positive, occurs either at the boundary of the WFW or at the zero orientation when maximum forces are applied. As a preliminary step, it is proven that  $F_1 > F_2$  is necessary when  $K_r > 0$  and  $\theta_r > 0$  in Appendix A.1. Using this result, the study of joint stiffness for  $\theta_r > 0$  is conducted in Appendix A.2. Though this study is confined to the positive half of the WFW, the results are applicable equally well on the negative half due to symmetry of the joint (see Section 3).

#### A.1. Proof for $(F_1 > F_2)$ when $K_r > 0$ and $\theta_r > 0$

Since  $K_r$  must be positive for all admissible combinations of forces inside the WFW, it is necessary that  $K_r(\theta_r = 0, F_1 = 0, F_2 = 0) > 0$ . From Eq. (5), this leads to the condition:  $C > 0$ . From the expression of  $C$  in Eq. (3), this requires  $(r > h)$  to be satisfied.

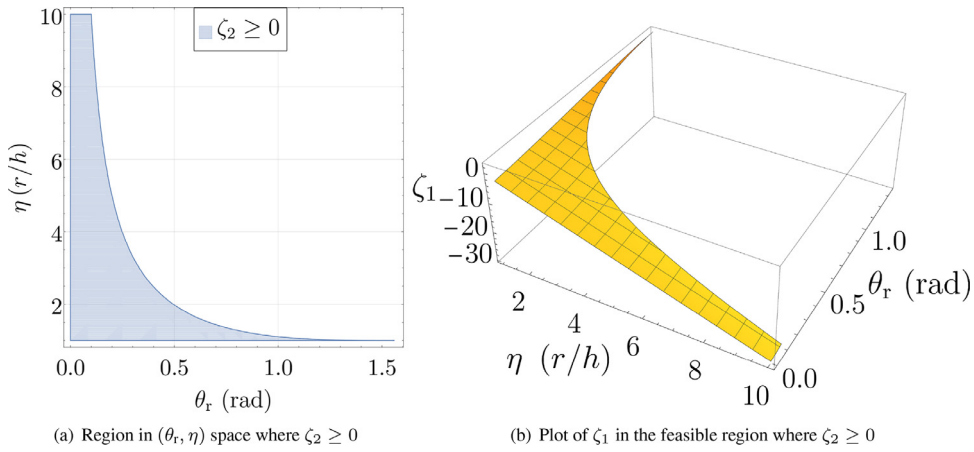


**Fig. A.19.** Plot of feasible region in  $(\theta_r, \eta)$  space and variation of  $\zeta_1$  inside this region.

The static equilibrium equation (Eqs. (3) and (4)) and stiffness expression (see Eq. (5)) can be rewritten in a simplified form as follows:

$$2Ccs - rF^-c - hF^+s = 0 \quad (\text{A.1})$$

$$K_r = C(c^2 - s^2) + \frac{1}{2}rF^-s + \frac{1}{2}hF^+c > 0 \quad (\text{A.2})$$

where  $c = \cos \frac{\theta_r}{2}$ ,  $s = \sin \frac{\theta_r}{2}$ ,  $F^+ = F_1 + F_2$ , and  $F^- = F_1 - F_2$ . Since it is known that the positive half of WFW must be limited by  $(\theta_r < \frac{\pi}{2})$  due to singularities, it is noted that  $(c > s)$ . Solving for  $F^+$  from Eq. (A.1) and substituting into the expression in Eq. (A.2), leads to the condition:

$$F^- > \frac{2Cs^3}{r} \quad (\text{A.3})$$

Since  $C > 0$  must be satisfied, it is clear that  $F^- > 0$ , or  $F_1 > F_2$ .

#### A2. Nature of the lower bound of $K_r$ when $\theta_r \geq 0$

Solving for  $F_1$  from the equation of static equilibrium (Eqs. (3) and (4)) results in:

$$F_1 = \frac{2Ccs + F_2(cr - hs)}{rc + hs} (\geq 0) \quad (\text{A.4})$$

Substituting for  $F_1$  from Eq. (A.4) into the expression of stiffness in Eq. (5) leads to:

$$K_{r2} = \frac{C(c^3r - hs^3)}{cr + hs} - \frac{F_2 hr}{cr + hs} \quad (\text{A.5})$$

Similarly, solving for  $F_2$  from the equilibrium equation and substituting into the expression of stiffness results in:

$$F_2 = \frac{-2Ccs + F_1(cr + hs)}{cr - hs} (\geq 0) \quad (\text{A.6})$$

$$K_{r1} = \frac{C(c^3r + hs^3)}{cr - hs} - \frac{F_1 hr}{cr - hs} \quad (\text{A.7})$$

From the expressions of stiffness in Eqs. (A.5) and (A.7), it is observed that the coefficients of  $F_2$  and  $F_1$  are both negative in the respective equations. This shows that the applied forces  $F_1$  and  $F_2$  have a negative impact on the stiffness of the R-joint. Thus, the minimum value of stiffness is achieved when at least one of the applied forces attains its maximum value of  $F_{\max}$ . Since it has been established in Appendix A.1 that  $F_1$  must be greater than  $F_2$  in the positive half of the WFW,  $F_1 = F_{\max}$  must be considered in this case. Thus, the expression for lower bound of stiffness may be obtained by substituting,  $F_1 = F_{\max}$ , in Eq. (A.7), as follows:

$$K_{r1} = \frac{C(c^3r + hs^3)}{cr - hs} - \frac{F_{\max}hr}{cr - hs} \quad (\text{A.8})$$

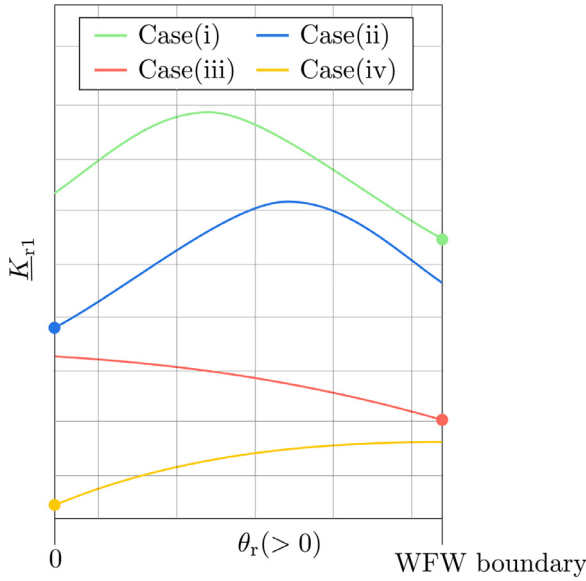


**Fig. A.20.** Possible cases for the lower bound of stiffness in the positive half of WFW.

In order to investigate the nature of  $\underline{K}_{r1}$ , its first-order and second-order derivatives w.r.t.  $\theta_r$  are computed:

$$\frac{d\underline{K}_{r1}}{d\theta_r} = \frac{C\{hr - 2cs(cr - hs)^2\}}{2(cr - hs)^2} - \frac{F_{\max}hr(ch + rs)}{2(cr - hs)^2} \quad (\text{A.9})$$

$$\begin{aligned} \frac{d^2\underline{K}_{r1}}{d\theta_r^2} = & -F_{\max} \frac{hr\{c^2(2h^2 + r^2) + 2chrs + s^2(h^2 + 2r^2)\}}{4(cr - hs)^3} \\ & + C \frac{-c^5r^3 + 3c^4hr^2s + c^3rs^2(r^2 - 3h^2) + c^2hs^3(h^2 - 3r^2) + ch^2r(3s^4 + 1) - h^3s^5 + hr^2s}{2(cr - hs)^3} \end{aligned} \quad (\text{A.10})$$

The stationary points of the lower bound of stiffness ( $\underline{K}_{r1}$ ) are obtained from the roots of  $(\frac{d\underline{K}_{r1}}{d\theta_r} = 0)$ . Further, the nature of these stationary points can be found by investigating the sign of  $\frac{d^2\underline{K}_{r1}}{d\theta_r^2}$  at those points.

Thus, solving for  $F_{\max}$  from (Eq. (A.9)=0) yields:

$$F_{\max} = \frac{C(hr - 2cs(cr - hs)^2)}{hr(ch + rs)} \quad (\text{A.11})$$

Substituting this result into Eq. (A.10), one obtains:

$$\frac{d^2\underline{K}_{r1}}{d\theta_r^2} = \frac{C\zeta_1}{4(c\eta - s)(c + \eta s)}, \text{ where, } \zeta_1 = (-2c^4\eta + 6c^3s + 8c^2\eta s^2 + 6c\eta^2s^3 - \eta - 2\eta s^4) \quad (\text{A.12})$$

with  $\eta = \frac{r}{h}$ . Recalling the conditions  $C > 0$  and  $(c > s)$  from Appendix A.1, it is clear that the first factor in the numerator and all the factors in the denominator of Eq. (A.12) are positive. Thus, the sign of  $\frac{d^2\underline{K}_{r1}}{d\theta_r^2}$  depends only on the sign of  $\zeta_1$ . It is observed that  $\zeta_1$  is a function of  $\theta_r$  and  $\eta$ , which could be positive or negative, in general.

Additionally, it is also necessary to account for the condition  $F_2 \geq 0$ , explicitly, on the lower boundary of stiffness and at the stationary points, since  $F_2$  was eliminated using the equilibrium equation. Thus, substituting  $F_1 = F_{\max}$  in Eq. (A.6) and using the expression of  $F_{\max}$  from Eq. (A.11), one obtains:

$$F_2 = \frac{C\zeta_2}{c + \eta s}, \text{ where, } \zeta_2 = \{-2c^4\eta(\eta^2 + 1)s + 2c^3\eta^2s^2 + c(\eta^2 - 2s^4 - 2\eta^2s^2) + \eta s\} \quad (\text{A.13})$$

It is observed that  $F_2 \geq 0$  requires  $\zeta_2 \geq 0$ .

In essence, one must study the nature of  $\zeta_1$ , while ensuring that  $\zeta_2 \geq 0$ . Since the corresponding expressions are quite complicated for algebraic analysis, further study is conducted through plots. The region in  $(\theta_r, \eta)$  space, where  $\zeta_2 \geq 0$  is

satisfied is shown in Fig. A.19(a). The plot of  $\zeta_1$  within this feasible region is shown in Fig. A.19(b). It is observed that  $\zeta_1$  is negative for all the admissible values of  $(\theta_r, \eta)$  considered and decreases with increasing value of  $\eta$ . This implies that, for any given  $\eta > 1$ , there can be at most one stationary point  $(\theta_r)$  for  $K_{r1}$ , within the positive half of WFW, and if it exists, it will be a maximum. Using this information, four possible cases are identified for the variation of  $K_{r1}$  against  $\theta_r$  as shown in Fig. A.20. In all of these cases, it is found that the minimum value of stiffness (highlighted by a large dot in Fig. A.20) always occurs at the zero orientation ( $\theta_r = 0$ ) or at the boundary of the WFW.

## Appendix B. Nature of lower bound of stiffness for X-joint

In this appendix, it is shown that the actuation forces have a *positive* impact on the stiffness of the X-joint and that the least value of stiffness, when it is imposed to be positive, occurs either at the boundary of WFW or at rest (zero orientation in the absence of forces). As in the case of R-joint, only the positive half of the WFW is considered in this study due to symmetry (see Section 3).

### B.1. Proof for ( $F_1 > F_2$ ) when $K_X > 0$ and $\theta_X > 0$

The equilibrium equation (Eqs. (8) and (9)) and the stiffness expression (see Eq. (10)) can be rewritten as follows:

$$\frac{bcF^+}{\sqrt{\lambda^2 - c^2}} - bcF^- + \frac{C_2 s(2c^2 - \lambda^2)}{\sqrt{\lambda^2 - c^2}} + 2csC_1 = 0 \quad (\text{B.1})$$

$$K_X = -\frac{bF^+(c^4 - c^2\lambda^2 + \lambda^2s^2)}{(\lambda^2 - c^2)^{3/2}} + bsF^- + 2C_1(c^2 - s^2) - \frac{C_2c\left\{(-c^2 + \lambda^2 + s^2)^2 - (\lambda^2 - 1)(c^2 - s^2)\right\}}{(\lambda^2 - c^2)^{3/2}} > 0 \quad (\text{B.2})$$

where  $F^+ = (F_1 + F_2)$ ,  $F^- = (F_1 - F_2)$ . In the context of X-joint,  $c = \cos \theta_X$ ,  $s = \sin \theta_X$ , and  $\lambda = \frac{l}{b}$ . Solving for  $C_1$  from Eq. (B.1) and substituting into the expression of stiffness in Eq. (B.2), results<sup>4</sup> in:

$$\frac{bc^2}{s}F^- - \frac{bc^2s^2}{(\lambda^2 - c^2)^{3/2}}F^+ - \frac{\lambda^4s^2}{c(\lambda^2 - c^2)^{3/2}}C_2 > 0 \quad (\text{B.3})$$

Since it is known that  $C_2 > 0$  (by definition in Eq. (8)) and  $F^+ > 0$ , it is observed that the second and third terms in Eq. (B.3) are both negative. On the other hand, the coefficient of  $F^-$  is found to be positive. Thus, in order to ensure that the left hand side of Eq. (B.3) remains positive,  $F^-$  must necessarily be positive. In other words, when the stiffness is specified to be positive, it is necessary that  $F_1 > F_2$  for the X-joint when  $\theta_X > 0$ .

### B.2. Nature of lower bound of $K_X$ when $\theta_X \geq 0$

Solving for  $F_1$  from the static equilibrium equation (Eqs. (8) and (9)), one obtains:

$$F_1 = \frac{bcF_2(\sqrt{\lambda^2 - c^2} + s) + 2csC_1\sqrt{\lambda^2 - c^2} + (2c^2 - \lambda^2)sC_2}{bc(\sqrt{\lambda^2 - c^2} - s)} (\geq 0) \quad (\text{B.4})$$

Substituting for  $F_1$  from the above equation into the expression of  $K_X$  in Eq. (B.2), leads to:

$$K_{X2} = \frac{2bc^2(\lambda^2 - 1)}{(\lambda^2 - c^2)(\sqrt{\lambda^2 - c^2} - s)}F_2 + \frac{2c^2(s\sqrt{\lambda^2 - c^2} - c^2 + \lambda^2 + s^2)}{\lambda^2 - c^2}C_1 \\ + \frac{\{c^2\lambda^2(s^2 - 3c^2) + c^2s(\lambda^2 - 2c^2)\sqrt{\lambda^2 - c^2} + 2c^4(c^2 - s^2) + \lambda^4\}}{c(c^2 - \lambda^2)\sqrt{\lambda^2 - c^2}}C_2 \quad (\text{B.5})$$

Similarly, solving for  $F_2$  from the equilibrium equation and substituting into the expression of  $K_X$  in Eq. (10) yields:

$$F_2 = \frac{bcF_1(\sqrt{\lambda^2 - c^2} - s) - 2csC_1\sqrt{\lambda^2 - c^2} - (2c^2 - \lambda^2)sC_2}{bc(\sqrt{\lambda^2 - c^2} + s)} (\geq 0) \quad (\text{B.6})$$

$$K_{X1} = \frac{2bc^2(\lambda^2 - 1)}{(\lambda^2 - c^2)(\sqrt{\lambda^2 - c^2} + s)}F_2 - \frac{2c^2(s\sqrt{\lambda^2 - c^2} + c^2 - \lambda^2 - s^2)}{\lambda^2 - c^2}C_1$$

<sup>4</sup> Alternatively, it is possible to eliminate  $F^+$  using Eq. (B.1), as in the case of R-joint. But, one must account for the condition:  $F^+ \geq 0$  along with the inequality from stiffness. This turned out to be difficult to handle, algebraically. On the other hand, since there are no constraints on the sign of  $C_1$  (see Eq. (8)), its elimination does not add any conditions other than the one from stiffness.

$$+ \frac{\{c^2\lambda^2(s^2 - 3c^2) - c^2 s(\lambda^2 - 2c^2)\sqrt{\lambda^2 - c^2} + 2c^4(c^2 - s^2) + \lambda^4\}}{c(c^2 - \lambda^2)\sqrt{\lambda^2 - c^2}} C_2 \quad (\text{B.7})$$

From the expressions of  $K_{X2}$  and  $K_{X1}$  presented above, it is observed that the coefficients of  $F_2$  and  $F_1$ , respectively, are always positive. This shows that the applied forces have a positive effect on the stiffness of the X-joint, contrary to what was observed for the R-joint. Thus, the lower bound for stiffness at a given orientation is obtained when at least one of the forces ( $F_1$  or  $F_2$ ) is equal to its minimum value of zero. Since it is known from Appendix B.1 that  $(F_1 > F_2)$  when  $(\theta_X > 0)$ , the lower bound of stiffness is obtained by substituting,  $F_2 = 0$  in Eq. (B.5):

$$\underline{K}_{X2} = \frac{2c^2(s\sqrt{\lambda^2 - c^2} - c^2 + \lambda^2 + s^2)}{\lambda^2 - c^2} C_1 + \frac{\{c^2\lambda^2(s^2 - 3c^2) + c^2 s(\lambda^2 - 2c^2)\sqrt{\lambda^2 - c^2} + 2c^4(c^2 - s^2) + \lambda^4\}}{c(c^2 - \lambda^2)\sqrt{\lambda^2 - c^2}} C_2 \quad (\text{B.8})$$

Further study on the nature of  $\underline{K}_{X2}$  is conducted by considering its first-order and second-order derivatives w.r.t.  $\theta_X$ :

$$\begin{aligned} \frac{d\underline{K}_{X2}}{d\theta_X} = & - \frac{2cC_1 \left[ -c^2\lambda^4 + 2 s\sqrt{\lambda^2 - c^2} \left\{ -c^2(\lambda^2 - c^2) + (\lambda^2 - c^2)^2 + \lambda^2 s^2 \right\} + (2\lambda^2 - c^2) \{c^4 + s^2(\lambda^2 - c^2)\} \right]}{(\lambda^2 - c^2)^{5/2}} \\ & + C_2 \left[ c^2\sqrt{\lambda^2 - c^2} \left\{ (\lambda^2 - c^2) \{ \lambda^2 - 2c^2(\lambda^2 - c^2) \} - 2c^2 s^2(2\lambda^2 - c^2) \right\} \right. \\ & \left. - s \{ \lambda^4(4c^4 - c^2 + \lambda^2) + 4c^2 \{ \lambda^2(\lambda^2(c^2 - s^2) + c^2 s^2) + 2c^4(c^2 - 2\lambda^2) \} \} \right] / \left[ c^2(\lambda^2 - c^2)^{5/2} \right] \end{aligned} \quad (\text{B.9})$$

$$\begin{aligned} \frac{d^2\underline{K}_{X2}}{d\theta_X^2} = & C_1 \left[ -8c^8 + 4c^6(5\lambda^2 + 2s^2) - 8c^4(2\lambda^4 + 5\lambda^2 s^2) + 4c^2\lambda^2(\lambda^4 - 3s^4 + 9\lambda^2 s^2) \right. \\ & - 2s\sqrt{\lambda^2 - c^2} \left\{ -4c^6 + 11c^4\lambda^2 + c^2\lambda^2(s^2 - 7\lambda^2) + 2\lambda^4 s^2 \right\} - 4\lambda^4 s^2(\lambda^2 + s^2) \Big] / [c^2 - \lambda^2]^3 \\ & + C_2 \left[ 2c^4 s\sqrt{\lambda^2 - c^2} (4c^6 - 12c^4\lambda^2 + 10c^2\lambda^4 - c^2\lambda^2 - 2\lambda^6 + \lambda^4 - 4\lambda^4 s^2) \right. \\ & + (\lambda^2 - c^2) \left\{ (28c^2 + 5)c^2\lambda^4 s^2 - \lambda^4 \{c^4 + (c^2 - 2)\lambda^2\} + 12c^4\lambda^2 s^2(3c^2 + s^2) \right. \\ & \left. \left. + 8c^6 \{2c^4 - c^2(2\lambda^2 + 1) + \lambda^4\} \right\} \right] / \left[ c^3(\lambda^2 - c^2)^{7/2} \right] \end{aligned} \quad (\text{B.10})$$

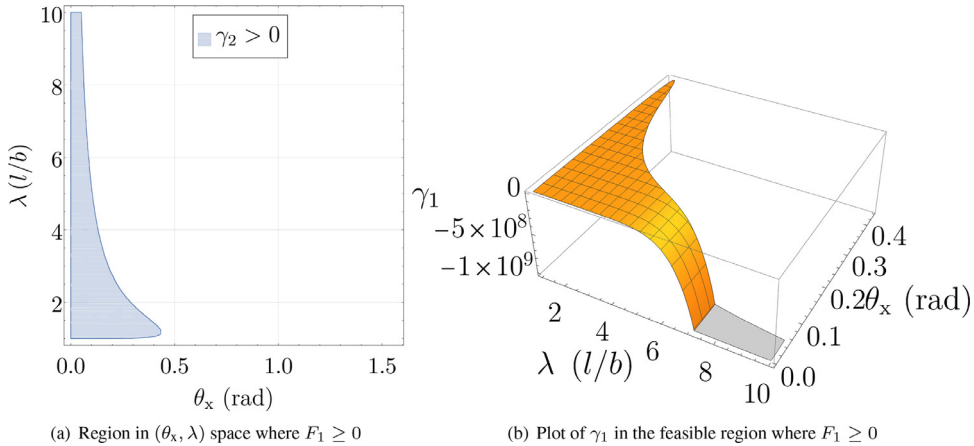
As in the previous case, the stationary points of  $\underline{K}_{X2}$  can be obtained from  $(\frac{d\underline{K}_{X2}}{d\theta_X} = 0)$ . The nature of these points can be found by studying the behavior of  $\frac{d^2\underline{K}_{X2}}{d\theta_X^2}$  at those points.

Thus, solving for  $C_1$  from (Eq. (B.9)=0) and substituting the result into Eq. (B.10), one obtains:

$$\frac{d^2\underline{K}_{X2}}{d\theta_X^2} = \frac{C_2\gamma_1}{c^3(\lambda^2 - c^2)^{5/2}\gamma_2} \text{ where,} \quad (\text{B.11})$$

$$\begin{aligned} \gamma_1 = & -8c^{16} + 2\lambda^8 s(s^2 + 2) \left( \lambda^2\sqrt{\lambda^2 - c^2} + s^2\sqrt{\lambda^2 - c^2} + \lambda^2 s \right) - c^2\lambda^6 \left\{ 8s^7\sqrt{\lambda^2 - c^2} + 4(2\lambda^2 + 1)s^5\sqrt{\lambda^2 - c^2} \right. \\ & + 32\lambda^2 s^3\sqrt{\lambda^2 - c^2} + 4\lambda^2(\lambda^2 + 3)s\sqrt{\lambda^2 - c^2} + 2\lambda^4 + 8\lambda^2 s^6 + 13\lambda^2 s^4 + \lambda^2(11\lambda^2 + 6)s^2 \Big\} \\ & + 4c^{14} \left( 8s\sqrt{\lambda^2 - c^2} + 3\lambda^2 + 2 \right) - 2c^{12} \left\{ -16s^3\sqrt{\lambda^2 - c^2} + (21\lambda^2 + 16)s\sqrt{\lambda^2 - c^2} - 4\lambda^4 + 6\lambda^2 - 4s^4 + 4s^2 \right\} \\ & - c^{10}\lambda^2 \left\{ 28s^3\sqrt{\lambda^2 - c^2} + 6(\lambda^2 - 7)s\sqrt{\lambda^2 - c^2} + \lambda^2(24\lambda^2 + 5) + 12s^4 + 4(4\lambda^2 - 3)s^2 \right\} \\ & + c^8\lambda^2 \left\{ 14s^5\sqrt{\lambda^2 - c^2} - 2(17\lambda^2 + 7)s^3\sqrt{\lambda^2 - c^2} + \lambda^2(26\lambda^2 + 3)s\sqrt{\lambda^2 - c^2} + \lambda^4(16\lambda^2 + 17) - 36\lambda^2 s^4 \right. \\ & + 4\lambda^2(5\lambda^2 + 9)s^2 \Big\} - c^6\lambda^4 \left\{ 40s^5\sqrt{\lambda^2 - c^2} + (29 - 82\lambda^2)s^3\sqrt{\lambda^2 - c^2} + 2\lambda^2(5\lambda^2 + 14)s\sqrt{\lambda^2 - c^2} \right. \\ & + \lambda^2(4\lambda^4 + 11\lambda^2 + 2) + 12s^6 + (3 - 64\lambda^2)s^4 + 77\lambda^2 s^2 \Big\} + c^4\lambda^6 \left\{ 48s^5\sqrt{\lambda^2 - c^2} + (53 - 36\lambda^2)s^3\sqrt{\lambda^2 - c^2} \right. \\ & \left. + (19\lambda^2 + 8)s\sqrt{\lambda^2 - c^2} + \lambda^2(3\lambda^2 + 4) + 20s^6 + (14 - 24\lambda^2)s^4 + (-4\lambda^4 + 48\lambda^2 + 2)s^2 \right\} \end{aligned} \quad (\text{B.12})$$

$$\gamma_2 = c^6 + c^2\lambda^2 \left( 6s\sqrt{\lambda^2 - c^2} + \lambda^2 + 3s^2 \right) - 2\lambda^2 s \left\{ (\lambda^2 + s^2)\sqrt{\lambda^2 - c^2} + \lambda^2 s \right\} - c^4 \left( 4s\sqrt{\lambda^2 - c^2} + 2\lambda^2 + s^2 \right) \quad (\text{B.13})$$

**Fig. B.21.** Plot of feasible region in  $(\theta_X, \lambda)$  space and variation of  $\gamma_1$  inside this region.

It is observed that all the factors except for  $\gamma_1$  and  $\gamma_2$ , are positive in  $\frac{d^2 K_{X2}}{d \theta_X^2}$ . Thus, the sign of  $\frac{d^2 K_{X2}}{d \theta_X^2}$  depends only on the signs of  $\gamma_1$  and  $\gamma_2$ .

As in the study of R-joint, the condition:  $F_1 \geq 0$  (see Eq. (B.4)) must be accounted for, explicitly, on the lower boundary of stiffness and at the stationary points. Thus, substituting  $F_2 = 0$  in Eq. (B.4) and eliminating  $C_1$  using the condition (Eq. (B.9)=0), one obtains:

$$F_1 = \frac{C_2 \lambda^4 s^2 [ \{ 2c^2(\lambda^2 - 1) - c^2 + \lambda^2 \} \sqrt{\lambda^2 - c^2} + c^2 s(\lambda^2 - c^2) ]}{bc^3 (\sqrt{\lambda^2 - c^2} - s) \gamma_2} \quad (\text{B.14})$$

where  $\gamma_2$  is defined in Eq. (B.13). It is observed that except for  $\gamma_2$ , all other factors are positive, when ( $\lambda > 1$ ). Thus, the condition  $F_1 \geq 0$  requires  $\gamma_2 > 0$  to be satisfied. Using this result, from Eq. (B.11) it is found that the sign of  $\frac{d^2 K_{X2}}{d \theta_X^2}$  purely depends on the sign of  $\gamma_1$ .

In essence, the sign of  $\gamma_1$  when  $\gamma_2 > 0$  must be studied. Since the expressions of  $\gamma_1$  and  $\gamma_2$  are quite complicated for algebraic analysis, further study is conducted through plots, as in the case of R-joint. The region in  $(\theta_X, \lambda)$  space where  $\gamma_2 > 0$  is plotted in Fig. B.21(a) and the surface plot of  $\gamma_1$  inside this region is shown in Fig. B.21(b). From these plots it is observed that  $\gamma_1$  is negative for all admissible values of  $(\theta_X, \lambda)$  considered and decreases with increasing  $\lambda$ . Thus, following the same line of arguments in the case of R-joint, there exists at most one stationary point for  $K_{X2}$  within the positive half of the WFW, and if it exists, it must correspond to a maximum. Hence, the least value of stiffness must occur either at the zero orientation or at the boundary of the WFW, for the X-joint.

### Appendix C. Treatment of the necessary condition: $A_{r_1} > 0$

From the expression of  $A_{r_1}$  in Eq. (29), the condition  $A_{r_1} > 0$  yields:

$$2\bar{k}(\eta^2 - 1) - \rho g \left( \sqrt{\eta^2 + 1} + 2\eta \right) > 0 \quad (\text{C.1})$$

$$\Rightarrow P(\eta^2 - 1) - \left( \sqrt{\eta^2 + 1} + 2\eta \right) > 0 \quad (\text{C.2})$$

where  $P = \frac{2\bar{k}}{\rho g}$ , is a function of the linear mass density of the material and upper bound of spring constant,  $\bar{k}$ . The necessary condition on  $P$  for the above inequality to be satisfied is derived in Appendix C.1. After ensuring the validity of that condition (i.e.,  $P > \underline{P}(\bar{\eta})$ ), the necessary condition on  $\eta$  can be derived as follows. Taking the second term in Eq. (C.2) to the right hand side and squaring both sides, results in:

$$(\eta^2 - 1)^2 P^2 + 3\eta^2 - 4(\eta^2 - 1)\eta P - 1 > 0 \quad (\text{C.3})$$

Since the left hand side of the above inequality is a quartic expression in  $\eta$  that does not factor out in the symbolic form, it is very difficult to obtain explicit conditions on  $\eta$  in terms of  $P$ . From several numerical examples, it is observed that the inequality in Eq. (C.3) reduces to a lower bound on  $\eta$  as:  $\eta > \underline{\eta}$ , where  $\underline{\eta}$  is the largest root of the quartic expression in Eq. (C.3). As a numerical illustration, consider  $\bar{k} = 2000$  N/m,  $\rho = 0.2121$  Kg/m and  $\theta_{rm} = 1$  radian. The corresponding

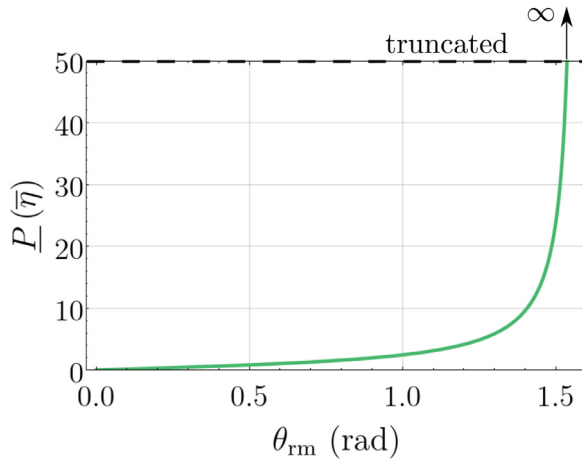


**Fig. C.22.** Variation of least feasible  $P$  with  $\theta_{rm}$ .

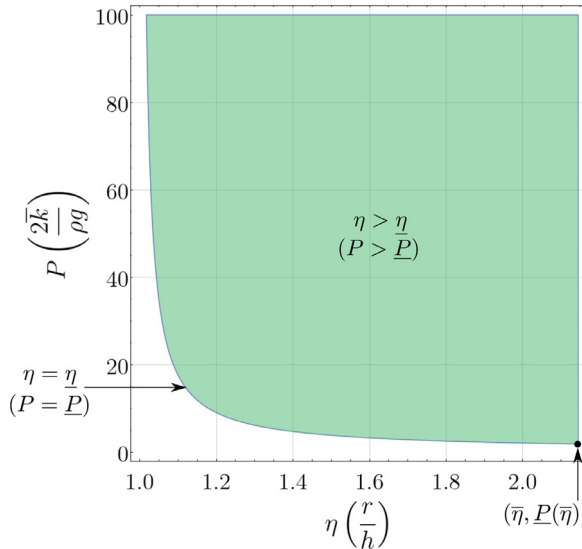


**Fig. C.23.** Feasible region in  $(\eta, P)$  space when  $\theta_{rm} = 1$  radian.

values of  $P = 1924.7763$  and  $\underline{\eta} = 1.0009$ . A plot highlighting the feasible region in  $(\eta, P)$  space is presented in Fig. C.23. It is observed that  $\underline{\eta}$  approaches unity with increasing value of  $P$ .

### C.1. Necessary condition involving $(\bar{k}, \rho, \theta_{rm})$

Rearranging the inequality in Eq. (C.2) one obtains a lower bound on  $P$  as:

$$P \geq \underline{P}, \text{ where } \underline{P} = \frac{\sqrt{\eta^2 + 1} + 2\eta}{\eta^2 - 1} \quad (\text{C.4})$$

The derivative of  $\underline{P}$  w.r.t.  $\eta$  is computed to be:

$$\frac{d\underline{P}}{d\eta} = -\frac{\eta^3 + 2\sqrt{\eta^2 + 1}\eta^2 + 2\sqrt{\eta^2 + 1} + 3\eta}{(\eta^2 - 1)^2 \sqrt{\eta^2 + 1}} \quad (\text{C.5})$$

which is clearly negative. This shows that  $\underline{P}$  decreases monotonically with  $\eta$ . Hence, a necessary condition for satisfying the inequality in Eq. (C.4) is that  $P$  be greater than the smallest  $\underline{P}$ , i.e.,  $P > \underline{P}(\eta = \bar{\eta})$ . From Eq. (13a), it is known that  $\bar{\eta} = \cot \frac{\theta_{rm}}{2} (= \frac{c}{s})$ , which upon substitution into the above condition yields:

$$P > \underline{P}(\eta = \bar{\eta}) \Rightarrow \frac{2\bar{k}}{\rho g} > \frac{(2c + 1)s}{c^2 - s^2} \quad (\text{C.6})$$

This condition involving  $(\rho, \bar{k}, \theta_{rm})$  must be satisfied necessarily for the existence of feasible designs. A plot of  $\underline{P}(\bar{\eta})$  against  $\theta_{rm}$  is shown in Fig. C.22. It is apparent that the value of  $\underline{P}(\bar{\eta})$  increases as the specified  $\theta_{rm}$  increases, which in turn means that the springs should be stronger (higher  $\bar{k}$ ) or the linear mass density ( $\rho$ ) must be smaller. Interestingly, the payload characteristics ( $M, d$ ) do not appear in these conditions.

#### Appendix D. Analysis of a quadratic inequality

Consider an inequality of the form:

$$A_x x^2 + B_x x + C_x \geq 0, \text{ with } (x \geq 0) \quad (\text{D.1})$$

The discriminant of the above expression is given by:

$$\delta_x = B_x^2 - 4A_x C_x \quad (\text{D.2})$$

It is known that the roots of the quadratic expression in Eq. (D.1) are:

$$x_1 = \frac{-B_x - \sqrt{\delta_x}}{2A_x}, \quad x_2 = \frac{-B_x + \sqrt{\delta_x}}{2A_x} \quad (\text{D.3})$$

Depending on the signs of  $(A_x, B_x, C_x)$ , the inequality in Eq. (D.1) will lead to different conditions on  $x (> 0)$  as illustrated in Table D.2.

**Table D.2**  
Reduction of the inequality in Eq. (D.1) to bounds on  $(x > 0)$ .

Case	Sign of $A_x$	Sign of $B_x$	Sign of $C_x$	Nature of roots/discriminant	Solution to Eq. (D.1)
1	+	+	+	Immaterial	Satisfied $\forall x > 0$
2a	+	-	+	$\delta_x \leq 0$	Satisfied $\forall x > 0$
2b	+	-	+	$\delta_x > 0 \Rightarrow x_1 > 0, x_2 > 0$	$(0 \leq x \leq x_1) \cup (x \geq x_2)$
3	+	+/-	-	$\delta_x > 0, x_1 < 0, x_2 > 0$	$x \geq x_2$
4	-	+/-	+	$\delta_x > 0, x_1 > 0, x_2 < 0$	$0 \leq x \leq x_1$
5a	-	+	-	$\delta_x < 0$	No solution
5b	-	+	-	$\delta_x \geq 0 \Rightarrow x_1 > 0, x_2 > 0$	$x \in [x_2, x_1]$
6	-	-	-	Immaterial	No solution

#### Appendix E. Expressions of the coefficients in Eqs. (33) and (57)

The expressions of symbols  $A_{r_2}, B_{r_2}, C_{r_2}$  used in Eq. (33) are listed below:

$$\begin{cases} A_{r_2} = (c^3 \eta - s^3) \left\{ 2(\eta^2 - 1)\bar{k} - g(\sqrt{\eta^2 + 1} + 2\eta)\rho \right\} \\ B_{r_2} = -g\eta M(c^3 \eta - s^3) \\ C_{r_2} = -\eta^2 \{ dgM(c^3 \eta - s^3) + K(c\eta + s) \} \end{cases} \quad (\text{E.1})$$

The coefficients in Eq. (57) for the cases  $i = 3, 4, 5$  are provided below:

$$\begin{cases} A_{b_3} = g(\lambda + 1)\rho \left\{ -2c^6\sqrt{\lambda^2 - 1} - c^2\lambda^2\sqrt{\lambda^2 - 1}(s\sqrt{\lambda^2 - c^2} + \lambda^2 + s^2) \right. \\ \left. - c^5(\lambda^2 - 2)(\sqrt{\lambda^2 - c^2} + s) + c^4\sqrt{\lambda^2 - 1}(2s\sqrt{\lambda^2 - c^2} + 3\lambda^2 + 2s^2) \right. \\ \left. + c^3(\lambda^2 - 2)(\lambda^2\sqrt{\lambda^2 - c^2} + s^2\sqrt{\lambda^2 - c^2} + \lambda^2 s) - \lambda^4\sqrt{\lambda^2 - 1}s^2 \right\} \\ B_{b_3} = gM \left\{ -2c^6\sqrt{\lambda^2 - 1} - c^2\lambda^2\sqrt{\lambda^2 - 1}(s\sqrt{\lambda^2 - c^2} + \lambda^2 + s^2) \right. \\ \left. - c^5(\lambda^2 - 2)(\sqrt{\lambda^2 - c^2} + s) + c^4\sqrt{\lambda^2 - 1}(2s\sqrt{\lambda^2 - c^2} + 3\lambda^2 + 2s^2) \right. \\ \left. + c^3(\lambda^2 - 2)(\lambda^2\sqrt{\lambda^2 - c^2} + s^2\sqrt{\lambda^2 - c^2} + \lambda^2 s) - \lambda^4\sqrt{\lambda^2 - 1}s^2 \right\} \\ C_{b_3} = c\sqrt{\lambda^2 - 1}K[-\lambda^2\sqrt{\lambda^2 - c^2} + c^2 \{ (\lambda^2 + 1 + s^2)\sqrt{\lambda^2 - c^2} + \lambda^2 s \} - c^4(\sqrt{\lambda^2 - c^2} + s)] \end{cases} \quad (\text{E.2})$$

$$\begin{cases} A_{b_4} = g(\lambda + 1)(\lambda^2 - 2)\rho \\ B_{b_4} = gM(-2 + \lambda^2) \\ C_{b_4} = \sqrt{\lambda^2 - 1}(4dgM + K) \end{cases} \quad (\text{E.3})$$

$$\begin{cases} A_{b_5} = g(\lambda + 1)\rho[2c^6 + c^2\lambda^2 \{ s(\sqrt{\lambda^2 - c^2} + s) + \lambda^2 \} - c^4 \{ 2s(\sqrt{\lambda^2 - c^2} + s) + 3\lambda^2 \} + \lambda^4 s^2] \\ B_{b_5} = gM[2c^6 + c^2\lambda^2 \{ s(\sqrt{\lambda^2 - c^2} + s) + \lambda^2 \} - c^4 \{ 2s(\sqrt{\lambda^2 - c^2} + s) + 3\lambda^2 \} + \lambda^4 s^2] \\ C_{b_5} = cK(\lambda^2 - c^2)^{3/2} - 4c^5 dgM(\sqrt{\lambda^2 - c^2} + s) + 4c^3 dgM(\lambda^2\sqrt{\lambda^2 - c^2} + s^2\sqrt{\lambda^2 - c^2} + \lambda^2 s) \end{cases} \quad (\text{E.4})$$

## References

- [1] V. Ramadoss, D. Zlatanov, M. Zoppi, Kinematic and workspace analysis of minimally routed cable driven open chains, in: T. Uhl (Ed.), *Advances in Mechanism and Machine Science, IFToMM WC*, 73, Springer, Cham, 2019, pp. 2841–2851, doi:[10.1007/978-3-030-20131-9\\_281](https://doi.org/10.1007/978-3-030-20131-9_281).
- [2] D.L. Bakker, D. Matsuura, Y. Takeda, J.L. Herder, Design of an environmentally interactive continuum manipulator, in: *Proceedings of the 14th IFToMM World Congress*, 2015, pp. 327–336, doi:[10.6567/IFToMM.14TH.WC.0513.114](https://doi.org/10.6567/IFToMM.14TH.WC.0513.114). Taipei, Taiwan.
- [3] M. Baril, T. Laliberté, F. Guay, C. Gosselin, Static analysis of single-input/multiple-output tendon-driven underactuated mechanisms for robotic hands, in: *Proceedings of the International Design Engineering Technical Conferences and Computers and Information in Engineering Conference Volume 2: 34th Annual Mechanisms and Robotics Conference, Parts A and B*, 2010, pp. 155–164, doi:[10.1115/DETC2010-28933](https://doi.org/10.1115/DETC2010-28933). Quebec, Canada.
- [4] Y. Mao, S.K. Agrawal, Design of a cable-driven arm exoskeleton (CAREX) for neural rehabilitation, *IEEE Trans. Rob.* 28 (4) (2012) 922–931, doi:[10.1109/TRO.2012.2189496](https://doi.org/10.1109/TRO.2012.2189496).
- [5] M. Azadi, S. Behzadipour, G. Faulkner, Antagonistic variable stiffness elements, *Mech. Mach. Theory* 44 (9) (2009) 1746–1758, doi:[10.1016/j.mechmachtheory.2009.03.002](https://doi.org/10.1016/j.mechmachtheory.2009.03.002).
- [6] Q. Boehler, M. Vedrines, S. Abdelaziz, P. Poignet, P. Renaud, Synthesis method for the design of variable stiffness components using prestressed singular elastic systems, *Mech. Mach. Theory* 121 (2018) 598–612, doi:[10.1016/j.mechmachtheory.2017.11.013](https://doi.org/10.1016/j.mechmachtheory.2017.11.013).
- [7] S. Wolf, G. Grioli, O. Eiberger, W. Friedl, M. Grebenstein, H. Höppner, E. Burdet, D.G. Caldwell, R. Carloni, M.G. Catalano, D. Lefeber, S. Stramigioli, N. Tsagarakis, M. Van Damme, R. Van Ham, B. Vanderborght, L.C. Visser, A. Bicchi, A. Albu-Schäffer, Variable stiffness actuators: review on design and components, *IEEE/ASME Trans. Mechatron.* 21 (5) (2016) 2418–2430, doi:[10.1109/TMECH.2015.2501019](https://doi.org/10.1109/TMECH.2015.2501019).
- [8] C. Zuo, J. Hong-zhou, A study of the planar serial-parallel mechanism with various stiffness for a biotic compliant fish, in: *Proceedings of the ASME International Mechanical Engineering Congress & Exposition*, 2013, pp. 13–21, doi:[10.1115/IMECE2013-62305](https://doi.org/10.1115/IMECE2013-62305). California, USA.
- [9] W. Zhao, A. Pashkevich, A. Klimchik, D. Chablat, Stiffness analysis of a new tensegrity mechanism based on planar dual-triangles, in: *Proceedings of the 17th International Conference on Informatics in Control, Automation and Robotics (ICINCO)*, SciTePress, 2020, pp. 402–411, doi:[10.5220/0009803104020411](https://doi.org/10.5220/0009803104020411).
- [10] B. Chen, Z. Cui, H. Jiang, Producing negative active stiffness in redundantly actuated planar rotational parallel mechanisms, *Mech. Mach. Theory* 128 (2018) 336–348, doi:[10.1016/j.mechmachtheory.2018.06.002](https://doi.org/10.1016/j.mechmachtheory.2018.06.002).
- [11] K. Li, H. Jiang, Z. Cui, Q. Huang, Variable stiffness design of redundantly actuated planar rotational parallel mechanisms, *Chin. J. Aeronaut.* 30 (2) (2017) 818–826, doi:[10.1016/j.cja.2016.07.001](https://doi.org/10.1016/j.cja.2016.07.001).
- [12] K.D. Snelson, Continuous tension, discontinuous compression structures, 1965, United States patent No. US3169611A.
- [13] R.E. Skelton, M. de Oliveira, *Tensegrity Systems*, Springer, United States, 2009, doi:[10.1007/978-0-387-74242-7](https://doi.org/10.1007/978-0-387-74242-7).
- [14] M. Arsenault, C.M. Gosselin, Kinematic, static, and dynamic analysis of a planar one-degree-of-freedom tensegrity mechanism, *J. Mech. Des.* 127 (6) (2005) 1152–1160, doi:[10.1115/1.1913705](https://doi.org/10.1115/1.1913705).
- [15] M. Arsenault, C.M. Gosselin, Kinematic, static and dynamic analysis of a planar 2-DOF tensegrity mechanism, *Mech. Mach. Theory* 41 (9) (2006) 1072–1089, doi:[10.1016/j.mechmachtheory.2005.10.014](https://doi.org/10.1016/j.mechmachtheory.2005.10.014).
- [16] A. Hamon, Y. Aoustin, S. Caro, On configurations of symbolic equations of motion for rigid multibody systems, *Multibody Syst. Dyn.* 31 (2014) 283–307, doi:[10.1007/s11044-013-9382-7](https://doi.org/10.1007/s11044-013-9382-7).
- [17] X. Zhang, H. Deng, X. Wang, C. Pan, H. Xu, Use of Anti-parallelogram Linkage Mechanism and Ordinary Gear Train for Power Transmission on a Rotary Engine, in: *Proceedings of the Third International Conference on Mechanic Automation and Control Engineering*, 2012, pp. 1041–1044.
- [18] B. Fasquelle, M. Furet, P. Khanna, D. Chablat, C. Chevallereau, P. Wenger, A bio-inspired 3-DOF light-weight manipulator with tensegrity X-joints, in: *Proceedings of 2020 IEEE International Conference on Robotics and Automation (ICRA 2020)*, 2020, Paris, France.
- [19] M. Furet, P. Wenger, Kinemostatic analysis and actuation strategy of a planar tensegrity 2-X manipulator, *J. Mech. Robot.* 11 (6) (2019), doi:[10.1115/1.4044209](https://doi.org/10.1115/1.4044209).
- [20] M. Furet, A. van Riesen, C. Chevallereau, P. Wenger, Optimal design of tensegrity mechanisms used in a bird neck model, in: B. Corves, P. Wenger, M. Hüsing (Eds.), *EuCoMeS 2018*, 59, Springer International Publishing, Cham, 2019, pp. 365–375, doi:[10.1007/978-3-319-98020-1\\_43](https://doi.org/10.1007/978-3-319-98020-1_43).
- [21] P. Wenger, M. Furet, Kinematic analysis of a planar manipulator with anti-parallelogram joints and offsets, in: J. Lenarčič, B. Siciliano (Eds.), *Proceedings of Advances in Robot Kinematics 2020*, Springer International Publishing, Cham, 2021, pp. 319–326, doi:[10.1007/978-3-03-50975-0\\_39](https://doi.org/10.1007/978-3-03-50975-0_39).
- [22] V. Muralidharan, P. Wenger, M. Furet, Static analysis and design strategy of two antagonistically actuated joints, in: D. Pisla, B. Corves, C. Vaida (Eds.), *New Trends in Mechanism and Machine Science, EuCoMeS 2020*, Springer International Publishing, Cham, 2020, pp. 459–469, doi:[10.1007/978-3-03-55061-5\\_52](https://doi.org/10.1007/978-3-03-55061-5_52).
- [23] C.M. Gosselin, Static balancing of spherical 3-DOF parallel mechanisms and manipulators, *Int. J. Rob. Res.* 18 (8) (1999) 819–829, doi:[10.1177/02783649922066583](https://doi.org/10.1177/02783649922066583).
- [24] D.A. Streit, B.J. Gilmore, ‘Perfect’ Spring equilibrators for rotatable bodies, *Trans. ASME J. Mech. Transm. Autom. Des.* 111 (4) (1989) 451–458, doi:[10.1115/1.3259020](https://doi.org/10.1115/1.3259020).
- [25] X. Diao, O. Ma, Q. Lu, Singularity analysis of planar cable-driven parallel robots, in: *Proceedings of the IEEE Conference on Robotics, Automation and Mechatronics*, 2008, pp. 272–277, doi:[10.1109/RAMECH.2008.4681507](https://doi.org/10.1109/RAMECH.2008.4681507).
- [26] V. Muralidharan, Wrench-feasible workspace and stiffness characteristics of revolute and antiparallelogram tensegrity joints, LS2N, École Centrale de Nantes, 2020 Technical report.
- [27] A. van Riesen, M. Furet, C. Chevallereau, P. Wenger, Dynamic analysis and control of an antagonistically actuated tensegrity mechanism, in: V. Arakelian, P. Wenger (Eds.), *ROMANSY 22-Robot Design, Dynamics and Control*, Springer International Publishing, Cham, 2019, pp. 481–490, doi:[10.1007/978-3-319-78963-7\\_60](https://doi.org/10.1007/978-3-319-78963-7_60).
- [28] R.K. Bansal, *A Textbook of Strength of Materials*, 4 ed., Laxmi Publications (P) Ltd, New Delhi, 2009.